Regional Tectonic Stress in Western Washington from Focal Mechanisms of Crustal and Subcrustal Earthquakes

by

Li Ma

A thesis submitted in partial fulfillment
of the requirements for the degree of

Master of Science

University of Washington

1988

Approved by Robert S Crosson
(Chairperson of Supervisory Committee)

Program Authorized
to Offer Degree GEOPHYSICS PROGRAM

Date MARCH 18, 1988

Master's Thesis

In presenting this thesis in partial fulfillment of the requirements for a Master's degree at the University of Washington, I agree that the Library shall make its copies freely available for inspection. I further agree that extensive copying of this thesis is allowable only for scholarly purposes, consistent with "fair use" as prescribed in the U.S. Copyright Law. Any other reproduction for any purposes or by any means shall not be allowed without my written permission.

Signature _____

Date _____

TABLE OF CONTENTS

LIST OF TABLES

LIST OF FIGURES

ACKNOWLEDGEMENTS

Many individuals have helped me during the course of my thesis research and I wish to thank them for their assistance. Robert Crosson gave me financial support and some crucial guidance. I would like to thank Ken Creager for some very useful suggestions, and both Ken and Tony Qamar for very helpful discussions. Ruth Ludwin helped me organize the data-base and improve my use of English in this thesis. Thanks to John Gephart who provided the basic software. I want to thank my friends Jonathan Lees, John VanDecar, David Lapp and Dai McClurg for their help and encouragement in my work. Finally I am very grateful to my dear husband T. Zhang for his deep love which fills my life with happiness and confidence.

This work was supported under grant numbers 14-08-0001-G1080, and 14-08-0001-G1390 by U.S. Geological Survey. Thanks for the finance.

Chapter 1

Introduction

The understanding of the subduction of the Juan de Fuca plate beneath the North American plate has greatly improved since the net convergence across the boundary was discovered in 1970 (Atwater, 1970). Magnetic anomaly patterns and analyses of the plate relative motion (Atwater, 1970; Riddihough, 1984) indicate that the Juan de Fuca plate converges with the North American plate in a N50°E direction and is subducted beneath it. Subcrustal seismicity defines a Benioff zone dipping nearly eastward at about 10°-12° in the Puget Sound area (Crosson, 1983; Taber and Smith, 1985). The slab dip angle varies from 10°-12° in the Puget Sound area to 15°-20° north and south of Puget Sound (Green, *et al.*, 1986; Keach, *et al.*,1986). A recent study of slab geometry suggests that the variation of dip angle is due to an up-arch of the slab beneath Puget Sound (Crosson and Owens, 1987).

Studies of focal mechanisms in western Washington show perhaps unexpected pattern of apparent stress. In central Puget Sound, composite plots of P and T axes from focal mechanisms for microearthquakes show apparent compressional axes oriented NS (Crosson, 1972; Yelin, 1982; Yelin and Crosson, 1982). In the Mount Rainier area, two crustal earthquakes which occurred in 1973 and 1974 have focal mechanisms similar to those in Puget Sound (Crosson and Frank, 1975; Crosson and Lin, 1975). The focal mechanisms in eastern Washington present NS P axes, too (Melon, 1975). Therefore, NS compression appears to be the dominant stress in the Pacific Northwest (Sbar, 1982 and 1983). However, in southwest Washington many focal mechanisms on the St. Helens Fault Zone

indicate apparent NE compression (Weaver and Smith, 1983). The Elk Lake earthquake on February 14, 1981 (M_b = 5.5) also has a NE P axis, consistent with the direction of the slab subduction and possibly indicating direct control from subduction.

The subcrustal stress state, up to now, has been far from clear because of the low rate of seismicity. The 1965 Seattle earthquake has a focal mechanism with an eastward dipping T axis (Langston and Blum, 1977), and a depth of 59 km (Algermissen and Harding, 1965). This could indicate an extensional stress parallel to the direction of subduction (Isacks and Molnar, 1971). Slab focal mechanisms on the Olympic Peninsula show P axes normal to the slab and T axes which display a range of angles within the slab with the average T axis in the down-dip direction (Taber and Smith, 1985). In Puget Sound, only a few subcrustal focal solutions has been published (Yelin, 1982), and are not sufficient to delineate the stress pattern in the slab.

Substantial progress has been made in understanding and interpreting focal mechanisms in terms of regional stress. Mckenzie (1969) pointed out that if slip occurs on preexisting zones of weakness, there may be substantial deviation between the directions of seismic P and T axes and the true principal axes of stress. He established the theoretical framework for analyzing the problem. A number of workers, among them Angelier (1979), have developed methods of analyzing geologic data such as fault striations in term of regional stress. Ellsworth and Zhonghuai (1980) have extended these methods to the analysis of focal mechanisms. Recently, Gephart and Forsyth (1984) have developed a complete and self-consistent method of inverting a population of focal mechanism data from a number of earthquakes in the source region for the orientation of the regional stress tensor and the relative magnitudes of principal stress. The method may be viewed as a test of the hypothesis of a uniform regional stress using focal

mechanism data. The purpose of this thesis is to take advantage of this significant advance in analyzing the large amount of high quality data now available in western Washington. In this thesis one hundred and ninety one focal mechanism solutions for western Washington earthquakes are analyzed. These events range in magnitude from 1.0 to 4.3. Forty-two are in the slab. The aim of this thesis is to investigate the crustal and subcrustal stress state in western Washington using high quality focal mechanism solutions.

A single focal mechanism only weakly constrains the ambient stress field (Mckenzie, 1969) due to the possibility that slip occurs on preexisting planes of weakness. Therefore, the inversion method of Gephart and Forsyth (1984) for determining the regional stress tensor using a large set of focal mechanisms is applied to both crustal and subcrustal earthquakes. The results of stress inversion indicate a difference of stress state between the crust and the subcrust. Horizontal north-south compression is the major characteristic of tectonic stress in the crust of western Washington. Deep focal mechanisms were examined in an attempt to interpret the state of stress within the subducted Juan de Fuca slab. Clear difference between the state of stress in the subducted slab versus that in the overlying continental plate is confirmed, however no simple stress state in the subducted slab can be identical. The analysis of stress state should be helpful in formulating a model to be used in the estimation of earthquake hazard in western Washington.

Chapter 2

Focal Mechanisms in Western Washington

Data Selection and Reduction

Since 1980 the seismograph network in Pacific Northwest has been much improved due to the installation of PDP 11/34 and PDP 11/70 computers at the University of Washington and the expansion of the network itself. Ninety-four short period, vertical-component, telemetered seismographs, one three-component World Wide Standardized Seismograph Network station, and two horizontal component Wood-Anderson seismographs were operated in 1980 (Qamar, *et al.* 1987). Figure 2.1 is a location map of stations. P3, C3, S3, N3 and E3 correspond to different velocity models for Puget Sound, Cascades, Mount St. Helens, Northern Washington and Eastern Washington. The earthquakes located in the P3, C3 and S3 regions are referred to as western Washington events in this thesis. The three velocity models are listed in Table 2.1. P3 was modified in 1985 (Qamar, *et al.*, 1987) by eliminating the low velocity zone in Crosson's earlier model (Crosson, 1976). All earthquakes which occurred before 1985 were relocated using these recent models.

Though in the general case, at least 10 cataloged first motions are necessary to determine an unambiguous focal mechanism (Yelin, 1982), all western Washington earthquakes which had eight or more polarities read in routine processing from 1982 to 1985 were examined. Compared with other subduction zones the seismicity within the slab under western Washington is relatively low. Deep earthquakes (depth > 30 kilometers) are not as common as the shallow ones.

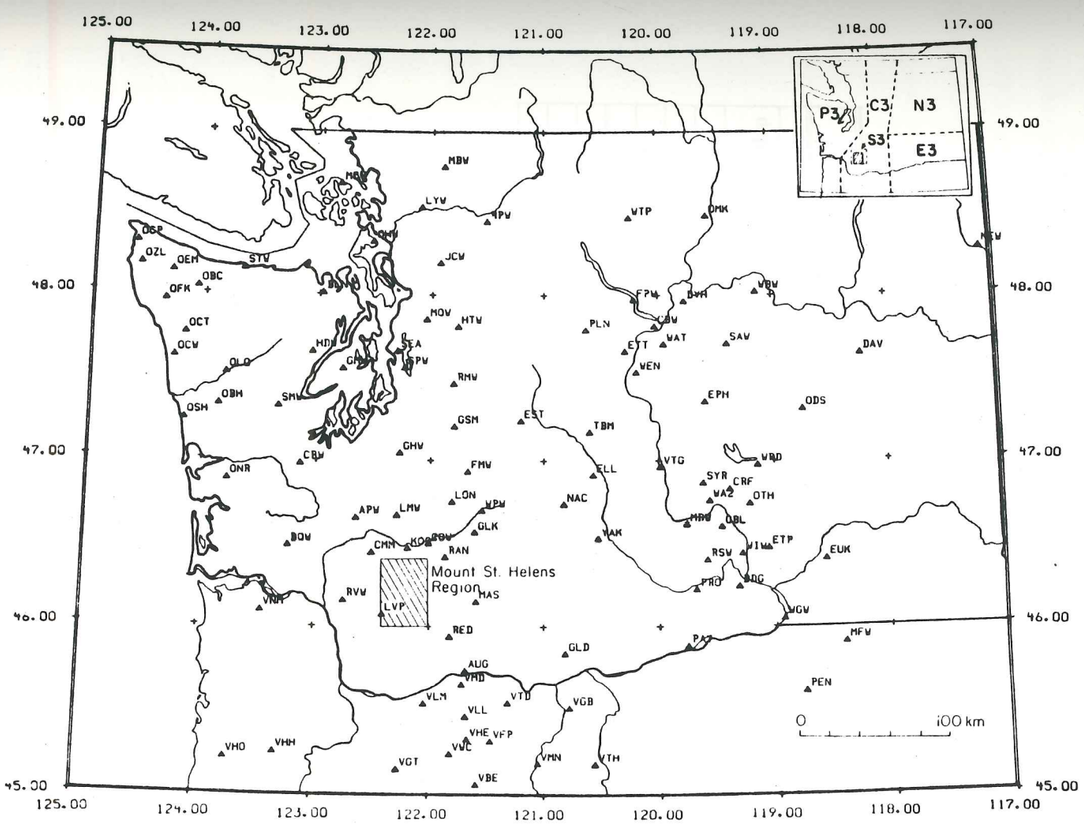

Figure 2.1. Location map for seismograph stations operated in 1980 (Qamar, *et al.*, 1986). The inset is a designation of different crustal velocity models for locating hypocenters. The regions defined by P3, C3 and S3 are referred to as "western Washington".

TABLE 2.1 Velocity Models for Western Washington

Cascades		St. Helens		Puget Sound	
depth range (km)	**velocity** (km/sec)	**depth range** (km)	**velocity** (km/sec)	**depth range** (km)	**velocity** (km/sec)
0.0-1.0	5.1	0.0-2.0	4.6	0.0-4.0	5.40
1.0-10.0	6.0	2.0-3.4	5.1	4.0-9.0	6.38
10.0-18.0	6.6	3.4-6.0	6.0	9.0-16.0	6.59
18.0-34.0	6.8	6.0-10.0	6.2	16.0-20.0	6.73
34.0-43.0	7.1	10.0-34.0	6.6	20.0-25.0	6.86
43.0-∞	7.8	34.0-43.0	7.1	25.0-41.0	6.95
		43.0-∞	7.8	41.0-∞	7.80

Aside from two significant events, one in 1949 (Hodgson and Storey, 1954), and the other in 1965 (Algermissen and Harding, 1965), only a few deep focal mechanisms were available previously (Crosson, 1983; Yelin, 1982 and Taber, 1985). In addition to using routinely processed data, a special effort was made to include all possible deep earthquakes by carefully examining the trace data of all deep events from 1980 through 1985 which had ten or more *P* arrivals.

Before determining a focal mechanism, the following criteria were used to select well-located earthquakes:

(1) Azimuthal gap is less than 100 °;

(2) Nearest station is within 100 km;

(3) Travel time residual (rms) is equal to or less than 0.3;

(4) Magnitude of earthquake is equal to or greater than 1.0.

In the procedure of determining focal mechanism some discrepancies of polarities were noticed. If the discrepancy was caused by a polarity reversal at the station in a certain time period, it was corrected by reversing the observed polarity. On average, errors in polarity affected less than 10% of the readings. earthquakes having polarities consistent with multiple solutions or having one nodal plane could be moved more than 20 ° were discarded for the further stress analysis.

Focal Mechanisms

After carefully examining and checking, 191 well constrained focal mechanisms in western Washington were constructed by hand fitting. These are listed in Table 2.2 and lower hemisphere equal area plots are shown for all events in the Appendix. The magnitude range of these events is from 1.0 to 4.3, and 149 are located at crustal depths. There are twenty-five earthquakes with magnitudes ≥

Table 2.2. List of Earthquakes

#	Date	Lat	Lon	Depth	Mag.	P-axis		T-axis		Plane A		Plane B	
						az.	pl.	az.	pl.	az.	pl.	az.	pl.
1	800204	47.39	121.65	96.35	2.4	55	85	236	5	326	40	146	50
2	800416	48.19	122.90	50.10	3.8	258	6	164	36	307	61	205	70
3	800608	47.97	123.10	48.54	4.2	272	84	15	1	99	44	291	47
4	800816	47.39	123.26	43.11	2.3	228	55	111	17	238	38	358	68
5	800906	47.54	123.42	46.16	2.8	173	68	62	8	175	41	315	56
6	801106	47.91	123.17	45.56	2.9	201	34	106	8	238	61	338	73
7	801130	47.35	123.34	43.81	2.6	130	20	32	20	171	61	81	90
8	810111	47.39	123.47	40.58	1.8	90	7	209	76	194	39	349	53
9	810704	47.86	122.73	52.11	2.8	303	31	47	22	88	51	353	84
10	810705	47.56	123.68	39.13	2.0	55	27	216	62	164	19	318	72
11	810722	47.96	123.43	44.18	2.3	227	64	89	20	205	29	346	67
12	810804	47.69	123.13	43.85	1.9	0	71	123	11	194	37	46	57
13	810821	47.62	123.67	40.52	2.8	180	85	0	5	90	40	270	50
14	820102	47.37	122.39	14.47	2.7	162	4	72	6	207	83	117	89
15	820114	48.10	122.81	55.95	2.7	254	65	74	25	164	20	344	70
16	820123	46.39	122.28	9.45	2.9	40	0	130	0	355	90	85	90
17	820123	46.61	121.43	3.33	3.2	180	45	90	0	215	60	325	60
18	820127	46.42	122.26	8.09	2.1	43	16	155	53	170	41	288	68
19	820208	46.52	122.28	4.02	2.3	246	4	342	57	6	50	129	57
20	820217	46.41	122.32	10.61	1.7	34	0	124	0	349	90	79	90
21	820301	46.40	122.30	10.97	2.7	35	34	151	33	184	38	94	90
22	820301	46.42	122.30	11.33	1.8	212	19	108	35	255	50	157	80
23	820301	46.40	122.30	11.48	1.0	44	4	136	22	178	72	272	78
24	820302	46.39	122.30	11.40	2.0	40	20	143	33	178	51	274	82
25	820302	46.41	122.29	11.61	1.8	213	3	307	50	337	55	91	60
26	820303	45.99	122.44	11.78	2.1	30	0	120	0	345	90	75	90
27	820303	46.39	122.30	11.13	1.5	20	4	110	4	155	84	65	90
28	820306	46.38	122.28	11.24	2.6	28	28	134	27	171	49	81	89
29	820310	46.74	122.20	16.71	2.4	192	4	285	38	322	61	65	67
30	820310	47.33	122.71	26.79	2.9	16	0	106	0	331	90	61	90
31	820313	47.06	122.17	72.53	1.9	266	45	86	45	356	90	176	90
32	820316	46.41	122.33	12.65	1.7	24	4	291	34	73	64	333	70
33	820316	46.40	122.27	11.22	2.1	33	0	123	0	348	90	78	90
34	820320	46.39	122.33	11.60	2.4	208	21	306	20	347	60	257	89
35	820326	46.40	122.31	11.61	1.9	47	35	166	34	197	36	108	90
36	820401	46.38	122.25	11.94	2.2	38	12	135	30	173	60	270	78
37	820402	46.27	122.29	10.90	1.2	56	6	147	7	191	81	282	89
38	820404	46.57	122.48	19.53	1.9	182	38	89	4	218	61	322	68
39	820410	46.38	122.31	8.88	2.2	240	40	144	8	274	57	18	69
40	820412	46.38	122.28	12.01	2.0	35	0	125	0	350	90	80	90
41	820414	47.71	122.52	27.28	3.4	6	8	101	33	138	61	238	73
42	820417	46.37	122.25	9.14	1.7	45	0	135	0	0	90	90	90
43	820426	46.43	122.26	9.69	2.7	201	14	299	29	336	59	73	80
44	820521	46.41	122.07	2.92	1.5	75	75	255	15	345	30	165	60
45	820526	46.41	122.31	11.94	1.8	35	0	125	0	350	90	80	90

Table 2.2 (continue)

#	Date	Lat	Lon	Depth	Mag.	P-axis		T-axis		Plane A		Plane B	
						az.	pl.	az.	pl.	az.	pl.	az.	pl.
46	820527	46.36	122.26	7.52	1.7	34	0	124	0	349	90	79	90
47	820528	46.40	122.32	11.56	1.7	45	0	135	0	0	90	90	90
48	820531	46.39	122.32	12.04	3.0	42	20	139	19	181	62	91	90
49	820531	46.40	122.28	11.76	1.8	27	32	139	31	173	42	83	90
50	820605	46.43	122.29	10.44	1.5	298	65	116	25	204	20	27	70
51	820606	46.41	122.25	10.86	1.0	45	0	135	0	0	90	90	90
52	820606	46.38	122.25	5.45	1.4	45	0	135	0	0	90	90	90
53	820704	46.35	122.30	9.26	1.2	212	33	328	34	359	39	90	89
54	820712	46.30	122.30	11.45	1.1	45	0	135	0	0	90	90	90
55	820718	46.58	121.39	6.48	2.9	5	0	95	0	320	90	50	90
56	820724	46.31	122.26	9.25	1.2	18	14	284	14	61	70	156	90
57	820819	46.40	122.25	9.68	2.3	38	20	136	20	177	61	267	90
58	820926	46.87	121.12	3.25	3.4	192	20	285	8	330	70	237	82
59	821008	46.28	122.08	0.77	2.2	168	75	348	15	78	30	258	60
60	821009	46.39	122.31	8.91	1.7	58	26	312	29	96	49	5	88
61	821015	47.59	122.63	27.52	3.0	38	18	284	51	89	40	334	71
62	821101	47.55	123.38	45.61	2.5	197	74	40	15	139	31	305	60
63	821112	47.69	122.69	24.54	2.8	6	0	96	30	137	69	235	69
64	821113	46.39	122.29	10.97	1.8	62	47	318	12	87	48	198	69
65	821116	46.31	122.30	10.58	1.9	38	0	128	0	353	90	83	90
66	821128	46.34	122.28	11.93	2.6	13	23	126	43	150	41	254	78
67	821211	47.53	122.73	20.22	2.3	5	17	101	18	143	65	233	89
68	821212	46.38	122.30	14.80	2.2	26	5	116	4	161	84	71	89
69	821212	46.28	122.50	15.85	1.9	8	13	98	0	144	81	52	81
70	821218	47.89	122.53	23.17	2.8	10	5	190	85	100	40	280	50
71	821220	46.59	121.42	5.26	2.7	15	37	108	4	158	61	56	68
72	821231	47.19	122.08	14.27	2.4	26	36	132	21	175	48	76	81
73	830124	47.11	121.99	6.62	3.0	342	15	162	75	72	30	252	60
74	830129	46.36	122.34	11.50	1.3	154	5	248	36	285	61	26	69
75	830131	46.67	122.33	17.91	2.2	358	0	88	66	110	50	246	50
76	830205	46.67	123.04	52.22	2.2	158	65	43	11	159	39	295	60
77	830208	46.44	122.33	9.25	1.2	40	13	133	12	177	72	86	89
78	830303	47.64	121.94	2.35	2.9	346	0	76	0	301	90	31	90
79	830309	46.40	122.29	11.36	1.1	200	35	299	12	345	56	245	75
80	830313	46.24	122.69	15.40	2.9	18	0	108	0	333	90	63	90
81	830315	46.52	122.79	24.05	2.7	36	46	127	0	182	59	71	60
82	830318	46.41	122.24	7.65	1.5	40	12	132	11	176	74	86	89
83	830320	46.12	122.13	9.12	2.0	207	5	299	22	341	71	75	78
84	830407	46.63	122.42	16.07	1.9	20	0	110	0	335	90	65	90
85	830409	46.74	121.82	8.27	1.8	170	7	272	60	289	46	56	58
86	830412	46.41	122.33	10.31	1.5	18	25	120	25	160	51	256	82
87	830412	46.39	122.31	8.61	2.0	32	30	123	1	171	68	73	70
88	830420	46.41	122.32	9.48	2.3	218	16	124	15	261	68	351	89
89	830420	46.41	122.33	9.27	2.3	38	10	130	11	174	75	264	89
90	830424	46.54	121.45	4.97	2.7	354	0	84	0	309	90	39	90

Table 2.2 (continue)

#	Date	Lat	Lon	Depth	Mag.	P-axis		T-axis		Plane A		Plane B	
						az.	pl.	az.	pl.	az.	pl.	az.	pl.
91	830425	47.28	123.56	38.31	1.9	99	31	7	4	138	66	237	71
92	830504	48.34	122.10	8.68	2.9	2	30	266	10	40	61	137	77
93	830506	46.41	122.23	7.41	2.3	38	0	128	0	353	90	83	90
94	830516	47.49	122.58	24.17	2.0	335	67	65	0	134	49	356	49
95	830519	47.64	122.50	23.48	2.0	28	0	118	62	143	51	273	51
96	830519	46.39	122.30	8.98	1.5	40	18	136	18	178	64	268	90
97	830521	47.36	121.49	11.69	2.8	163	11	256	14	299	72	30	88
98	830521	46.38	122.37	9.32	1.9	180	18	87	10	222	70	314	84
99	830525	47.78	121.71	10.72	3.0	180	16	275	16	317	67	231	90
100	830605	46.54	122.73	23.73	2.3	198	36	291	4	341	62	239	69
101	830708	47.76	123.02	47.12	2.4	144	55	281	27	332	25	208	75
102	830726	46.69	122.54	17.35	2.2	199	3	98	75	274	44	123	50
103	830728	46.06	122.81	16.06	2.4	20	0	110	57	139	54	261	54
104	830728	46.07	122.74	15.65	2.3	176	3	79	68	244	46	106	52
105	830802	47.66	122.87	48.48	2.3	254	85	74	5	164	40	344	50
106	830819	47.43	122.74	23.12	2.2	214	23	96	47	259	37	150	76
107	830828	48.00	122.87	51.50	3.9	75	16	345	0	119	79	211	79
108	830901	47.77	122.72	19.20	2.5	163	0	73	30	212	69	114	69
109	830902	46.33	122.53	15.94	1.0	49	45	306	13	76	49	185	70
110	830904	47.89	122.63	22.78	2.6	164	5	344	85	254	40	74	50
111	830914	47.09	121.93	19.02	2.2	161	60	295	22	353	29	220	69
112	830915	46.53	122.45	15.31	2.3	16	6	110	36	147	61	249	70
113	830929	47.34	122.72	27.12	2.7	184	2	276	40	312	61	57	65
114	831002	46.46	122.33	9.20	2.2	38	0	128	28	169	71	267	71
115	831023	46.56	122.35	17.28	2.5	212	7	111	58	272	47	147	59
116	831031	47.35	123.29	43.36	4.3	316	75	134	15	223	30	44	60
117	831101	46.34	122.29	9.95	2.0	155	32	259	21	300	51	205	83
118	831213	46.37	122.26	9.42	1.8	238	15	332	16	15	68	105	89
119	831216	47.34	122.03	12.91	3.0	214	8	305	10	350	77	80	89
120	840104	47.68	122.58	18.83	2.8	216	13	119	28	261	60	165	80
121	840105	47.44	122.28	38.77	1.9	108	4	287	86	198	41	18	49
122	840111	46.91	121.64	5.94	2.2	202	28	105	13	240	61	336	80
123	840111	46.41	122.28	6.52	1.7	27	0	117	0	342	90	72	90
124	840219	47.35	122.35	15.83	2.4	160	10	347	80	249	35	71	55
125	840223	47.65	123.04	46.32	2.2	117	48	16	10	143	50	255	66
126	840314	47.84	122.36	22.68	2.7	170	4	350	86	260	41	80	49
127	840323	47.75	122.69	19.07	2.9	174	0	84	0	39	90	309	90
128	840328	47.33	123.13	42.89	1.9	136	50	249	18	299	40	185	71
129	840404	46.43	122.32	9.21	2.4	24	10	135	64	141	41	274	59
130	840408	46.80	122.49	67.03	3.3	286	20	44	53	55	36	173	71
131	840427	47.65	122.03	9.77	2.9	147	0	57	13	193	81	101	81
132	840602	47.49	122.71	21.49	3.6	216	4	308	22	350	72	84	78
133	840602	47.50	122.72	22.60	2.8	26	8	290	38	75	58	332	70
134	840604	46.29	123.04	52.60	3.7	184	31	88	10	221	61	319	76
135	840619	47.72	122.99	8.78	3.0	0	0	90	0	315	90	45	90

Table 2.2 (continue)

#	Date	Lat	Lon	Depth	Mag.	P-axis		T-axis		Plane A		Plane B	
						az.	pl.	az.	pl.	az.	pl.	az.	pl.
136	840621	48.30	122.97	46.47	2.0	132	7	225	21	266	70	0	80
137	840708	47.57	122.81	46.69	2.2	307	35	128	55	35	10	217	80
138	840716	46.49	122.30	15.25	2.8	210	6	303	25	344	68	79	77
139	840724	47.77	122.45	21.28	2.7	4	7	118	73	111	40	261	54
140	840805	46.52	122.32	11.26	3.1	22	20	290	6	64	71	157	80
141	840812	47.73	123.02	46.32	2.2	112	0	22	43	166	61	58	61
142	840902	48.75	123.20	57.01	2.6	317	12	137	78	47	33	227	57
143	840905	47.92	122.04	17.37	2.2	322	5	212	76	38	42	244	51
144	840908	46.29	122.28	7.00	1.4	210	22	117	8	251	69	345	81
145	840915	46.50	122.40	13.36	1.1	26	12	119	12	162	73	72	90
146	840920	47.55	122.34	26.52	2.7	26	4	293	37	76	62	333	68
147	841016	46.43	122.31	10.58	1.2	0	25	180	65	90	20	270	70
148	841029	47.85	122.43	18.35	2.0	168	3	264	62	284	49	54	54
149	841103	46.41	122.32	11.24	1.9	0	25	180	65	90	20	270	70
150	841103	46.41	122.31	11.57	1.1	12	38	106	5	156	60	53	68
151	841120	47.95	121.98	16.64	2.0	310	13	212	30	355	59	258	79
152	841121	46.98	123.69	35.67	2.8	211	36	326	30	1	40	267	86
153	841130	47.76	122.24	23.72	2.7	178	28	85	6	218	66	315	75
154	841204	46.55	122.37	19.94	1.7	228	29	137	2	268	68	6	72
155	841217	47.31	122.91	46.30	3.2	236	29	131	25	272	50	4	88
156	841220	47.88	122.46	22.65	2.2	5	5	102	54	127	51	246	59
157	850121	46.91	122.02	12.80	2.7	176	3	296	84	272	42	81	48
158	850123	47.77	122.47	18.39	2.6	181	6	295	75	285	41	79	52
159	850123	47.83	122.48	18.44	2.2	177	6	300	79	277	40	79	52
160	850129	47.48	121.83	17.55	2.7	359	3	262	67	67	47	289	52
161	850306	48.90	122.82	66.48	1.8	41	21	145	32	179	51	275	83
162	850318	47.37	122.64	53.30	3.5	276	34	20	20	63	50	326	81
163	850321	47.64	122.22	7.86	3.0	160	12	257	29	295	60	31	79
164	850330	46.70	122.20	15.98	2.8	148	21	246	21	287	60	197	90
165	850330	46.69	122.20	16.69	2.6	155	0	65	0	20	90	290	90
166	850414	46.40	122.25	8.03	2.1	25	8	291	26	71	66	335	78
167	850417	47.70	122.25	23.94	1.9	184	18	297	50	314	40	68	71
168	850426	47.31	122.48	57.83	2.5	271	12	170	42	320	52	214	71
169	850426	48.41	122.31	18.21	3.0	182	35	2	55	272	10	92	80
170	850430	48.40	122.32	18.16	2.4	32	0	302	0	257	90	167	90
171	850430	46.41	122.30	10.95	2.0	37	27	143	29	180	49	271	89
172	850509	46.57	121.84	9.84	2.7	196	1	14	89	286	44	106	46
173	850521	47.66	123.22	47.22	2.8	113	22	213	24	253	56	344	89
174	850523	46.21	122.21	0.72	2.5	190	0	10	90	100	45	280	45
175	850523	47.67	123.31	47.04	2.0	33	6	125	21	167	71	261	80
176	850616	47.44	121.87	17.03	3.1	314	6	49	37	84	60	187	69
177	850621	46.51	122.37	20.02	1.8	212	40	310	9	359	56	255	70
178	850706	47.77	122.27	17.97	3.1	157	13	54	44	206	49	98	70
179	850801	46.26	122.52	16.91	1.4	13	7	277	40	63	57	318	68
180	850822	47.67	122.91	50.27	1.8	244	25	62	65	336	20	153	70

Table 2.2 (continue)

#	Date	Lat	Lon	Depth	Mag.	P-axis		T-axis		Plane A		Plane B	
						az.	pl.	az.	pl.	az.	pl.	az.	pl.
181	850905	46.33	122.23	7.16	2.5	9	11	101	11	145	74	55	90
182	850914	47.43	122.38	19.85	3.0	334	15	240	14	17	69	107	89
183	851006	47.93	122.90	19.96	2.8	322	0	52	70	71	48	213	48
184	851014	46.37	122.68	20.16	1.5	32	12	134	44	162	50	270	70
185	851017	47.46	123.00	15.87	2.6	178	0	268	67	289	49	67	49
186	851106	46.89	121.99	7.61	2.3	3	12	248	64	66	39	292	61
187	851115	47.51	123.59	42.13	2.7	270	76	90	14	180	31	0	59
188	851117	46.43	122.33	11.06	2.9	45	0	135	0	0	90	90	90
189	851202	49.06	123.58	59.40	2.3	173	62	60	12	179	40	310	61
190	851204	48.86	122.87	59.14	2.2	240	60	22	24	81	25	305	71
191	851227	46.97	121.94	7.02	3.0	346	3	255	19	32	74	299	79

3.0. Figure 2.2 shows the distribution of all shallow earthquakes with good focal mechanisms. Most earthquakes in the P3 area were located around Puget Sound. No shallow mechanisms were obtained on the Olympic Peninsula or along the coastline. In the Cascade area, most earthquakes were located in southern part. The distribution of deep focal mechanisms is shown in Figure 2.3. Most were located on the western side of Puget Sound and the eastern side of Olympic Peninsula. A few were located in southern Puget Sound and north, near the border of the United States and Canada. The cross section of Figure 2.4 shows the hypocenters of all earthquakes used. The distribution of earthquakes in the slab is not continuous. No focal mechanism were determined between 75 km and 90 km depth where the slab may change its dip angle.

Mechanisms of some individual deep earthquakes are worth noting. Two well determined deep focal mechanisms for the largest events in the data set (magnitude > 4.0) are shown in Figure 2.5. Each number on the left of the focal sphere matches that in Table 2.2 and in the Appendix. Event 3 located in the northeast corner of the Olympic Peninsula at 48.5 km depth. Event 116 located in the southern part of the Olympic Peninsula at 43.4 km depth. Both have vertical P axes and nearly horizontal T axes, with one T axis oriented north and the other oriented southeast. Focal mechanisms of lower magnitude events differ from these. In Figure 2.6 there are six focal mechanisms of events with magnitudes equal to or greater than 3.0, but less than 4.0. Event 2 and 107, located near event 3, have similar focal solutions, east-west P axes and north-south T axes. The directions of T axes almost match that of event 2, but the P axes are dissimilar, since event 3 has a vertical P axis while event 2 and event 107 have nearly horizontal P axes. Their depths are approximately 50 kilometers. Event 155 and event 162, located in the southern Puget Sound and near event 116 (Figure 2.5). Although the P axes of event 116 and 155 are discrepant, both T axes orient in a

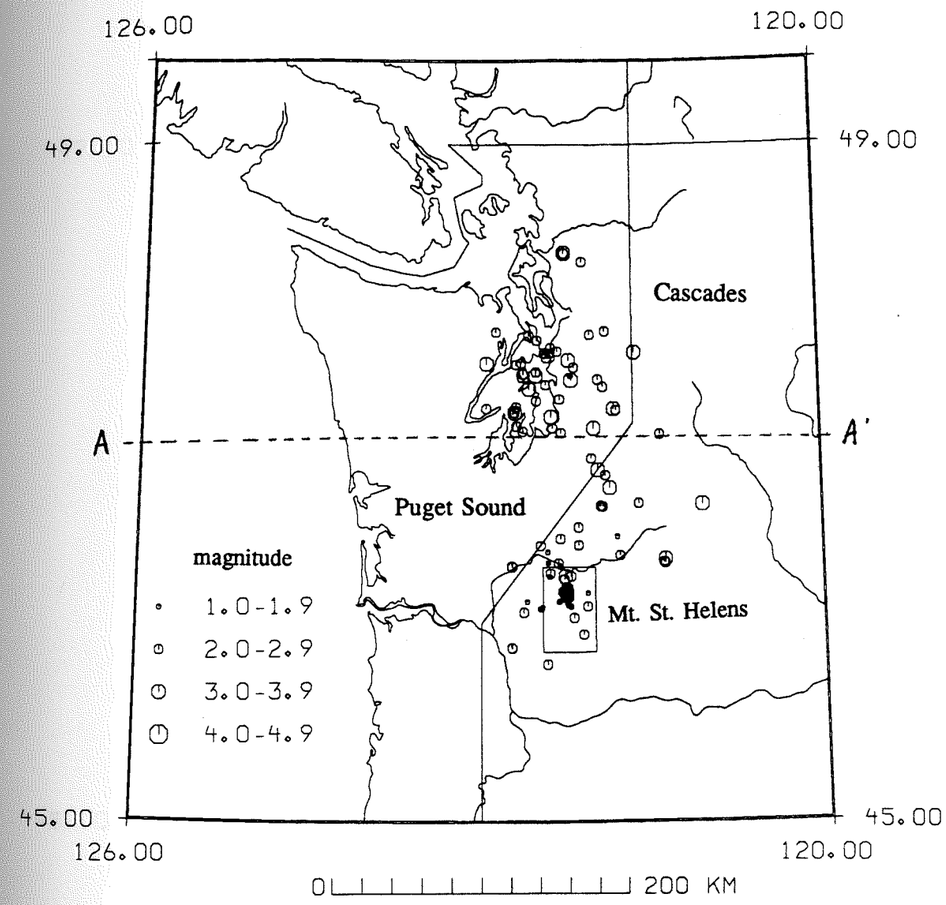

Figure 2.2. Map distribution of shallow earthquakes with good focal mechanisms in period 1982-1985.

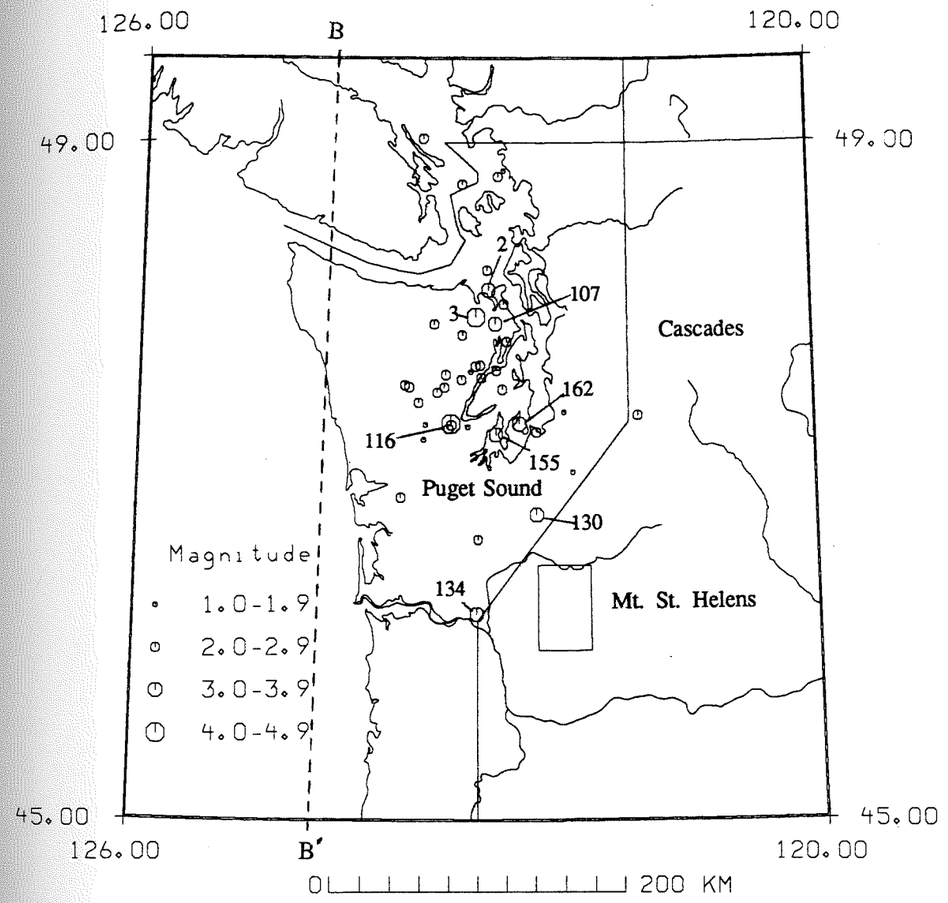

Figure 2.3. Map distribution of deep earthquakes with good focal mechanisms in period 1980-1985. The sequence numbers are marked for earthquakes with magnitudes equal to or greater than 3.0.

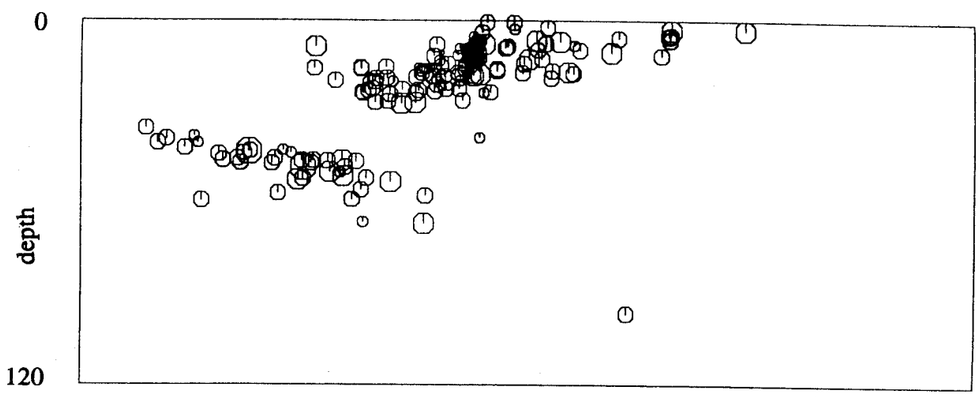

Figure 2.4. Cross section along dashed line $A - A'$ in Figure 2.3.

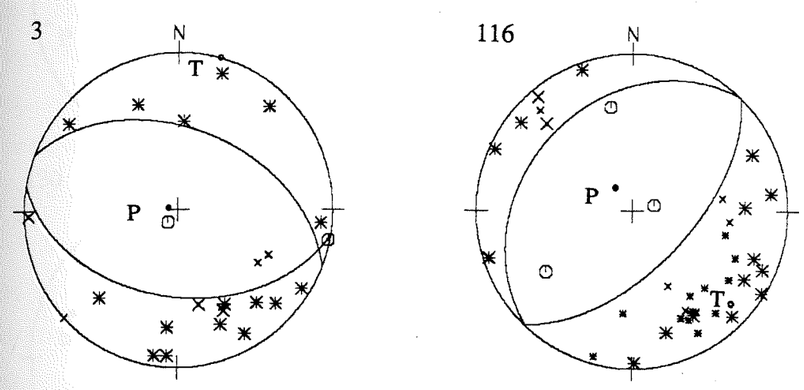

Figure 2.5. Two deep focal mechanisms with magnitudes greater than 4.0. P is the apparent compressional axis in dilatation quadrant and T is the apparent tensional axis in compression quadrant. The sequence number on the left shoulder of each focal sphere corresponds to that in Table 2.2 and in the Appendix.

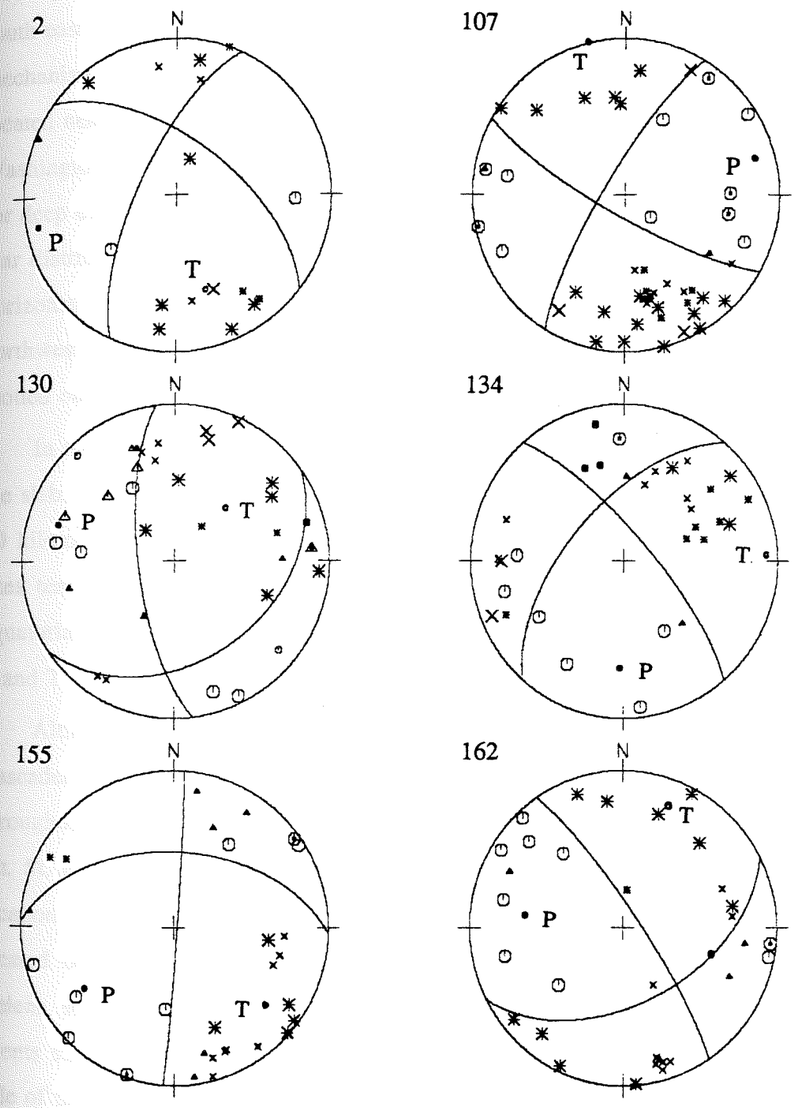

Figure 2.6. Six well constrained subcrustal focal mechanisms with magnitudes greater than 3.0.

south-east direction. Event 162 with depth in 53.3 km has a different focal mechanism from the other two southern Puget Sound events. Event 134, which located near Columbia River, and is the most southern deep earthquake in western Washington, has north-south P and east-west T. Composite plots of P and T axes for deep events are shown in Figure 2.7. Neither P axes nor T axes present a regular distribution on the focal sphere. P axes vary from near vertical to near near horizontal with the azimuth varying from northeast to southeast and from northwest to southwest, with few P axes directing north-south. All T axes are plotted out in mapview (Figure 2.8).

In the crust the focal mechanism solutions seem very different from those in the slab. There were 47 good focal mechanisms in shallow Puget Sound (depth ≤ 30 kilometers). The composite plots of P and T axes (Figure 2.9) show that P axes tend to be horizontal with north-south azimuth and T axes present a wide equatorial girdle distribution. In the Cascades, the patterns of composite plots of P and T axes are almost same as those in shallow Puget Sound (Figure 2.10).

Although there is similarity of focal mechanisms in Puget Sound and the Cascades area, it can not be deduced that the focal mechanisms are identical throughout the crust of western Washington. Figure 2.11 is an enlargement of the Mt. St. Helens area shown in Figure 2.2, with the smaller rectangle showing the location of volcanic cone. Among seventy-three focal mechanisms, only one located beneath the cone. Most of them located along the northern part of St. Helens seismic zone (Weaver and Smith, 1983), with some lower magnitude events scattered elsewhere. One earthquake with magnitude 3.0 was in the south side of the Cowlitz River and another earthquake with magnitude 3.1 had the same location as the 1981 Elk Lake earthquake. These two focal mechanisms are shown in Figure 2.12. Event 48 has a similar solution with that of 1981 Elk Lake mainshock (Weaver and Smith, 1983) which had a northeast P axis. The P axis of

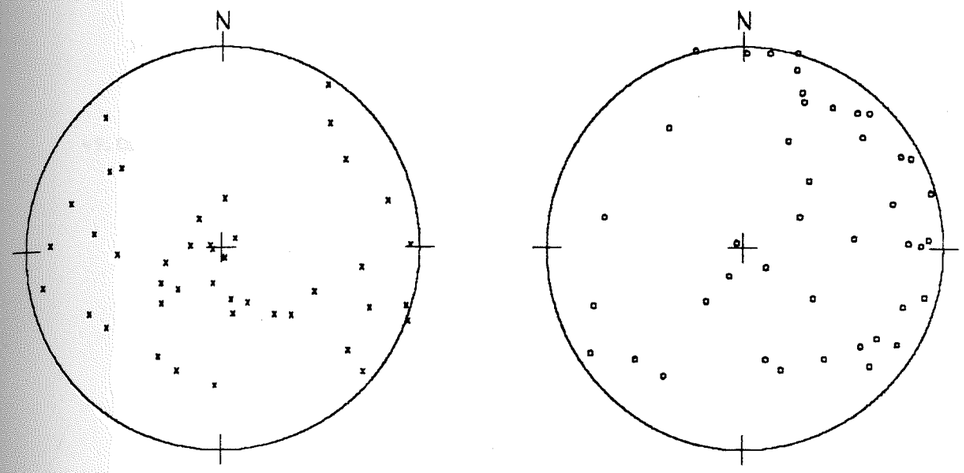

Figure 2.7. Lower-hemisphere, equal area projections of P (left) and T (right) axes from focal mechanisms of 42 subcrustal earthquakes (depth>35 km). All crosses are P axes, and all circles are T axes.

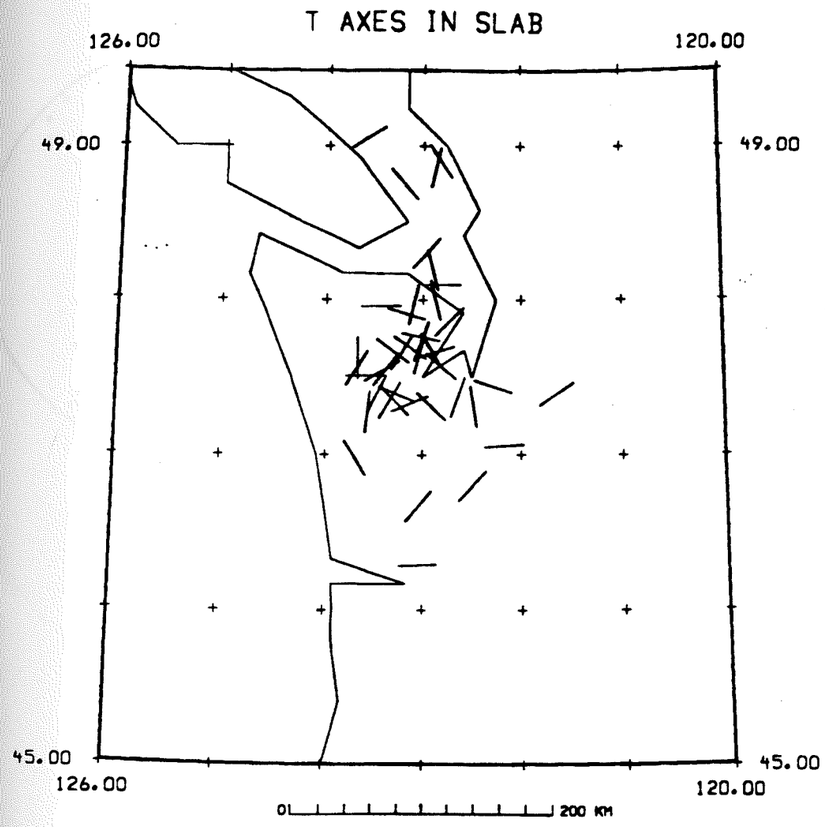

Figure 2.8. T axes from focal mechanisms of 42 subcrustal earthquakes on map.

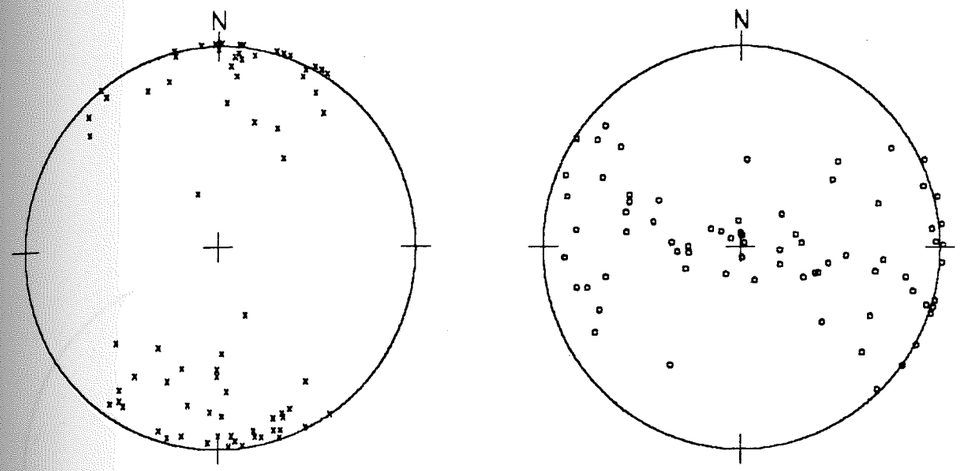

Figure 2.9. Lower-hemisphere, equal area projections of P (left) and T (right) axes from focal mechanisms of 47 shallow Puget Sound earthquakes (depth<35 km). All crosses are P axes, and all circles are T axes.

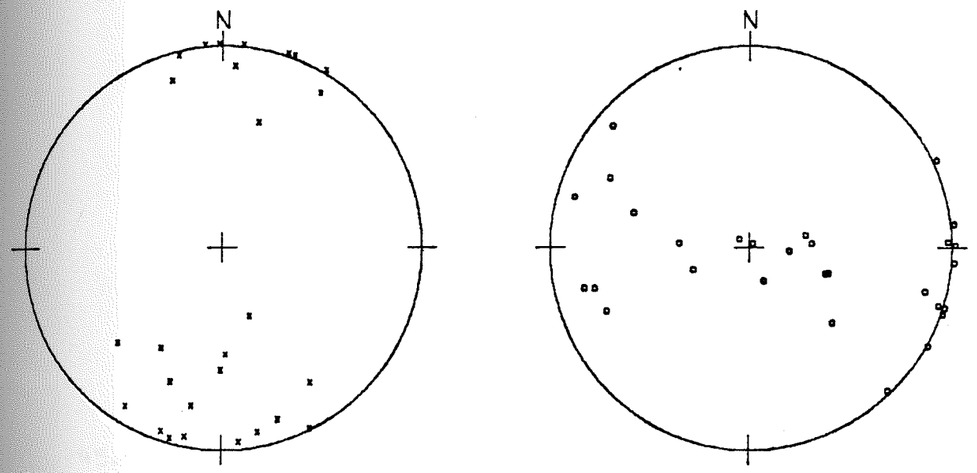

Figure 2.10. Lower-hemisphere, equal area projections of P (left) and T (right) axes from focal mechanisms of 29 shallow Cascades earthquakes (depth<35 km). All crosses are P axes, and all circles are T axes.

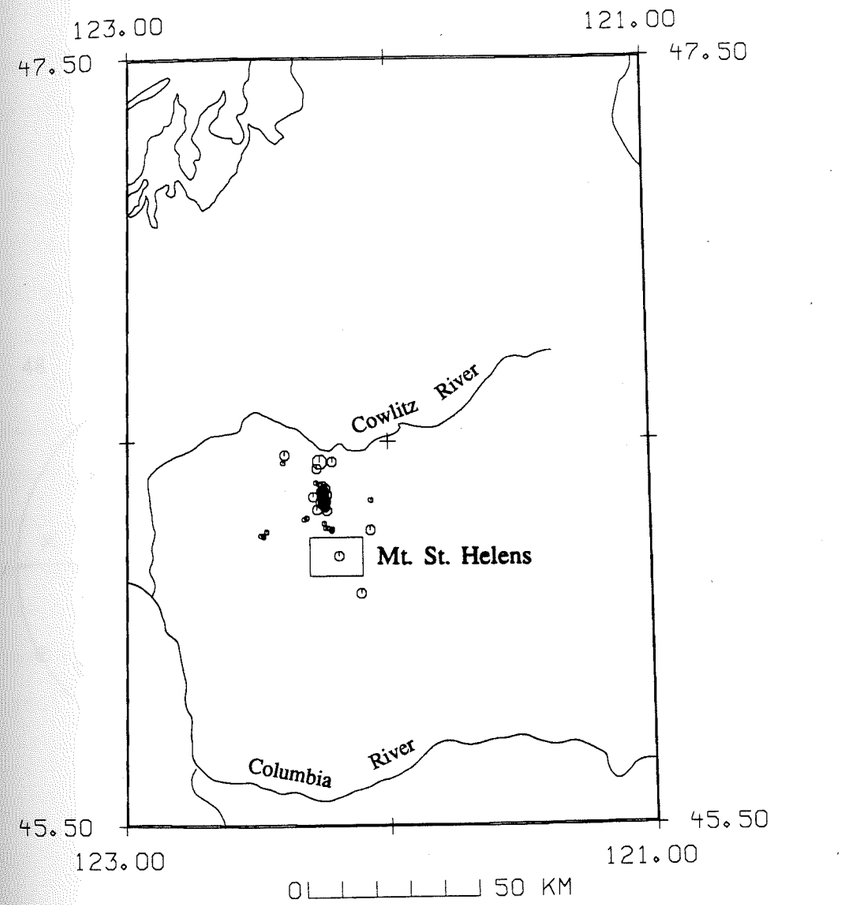

Figure 2.11. Map distribution of Mt. St. Helens earthquakes. The small rectangular is the location of Mt. St. Helens cone.

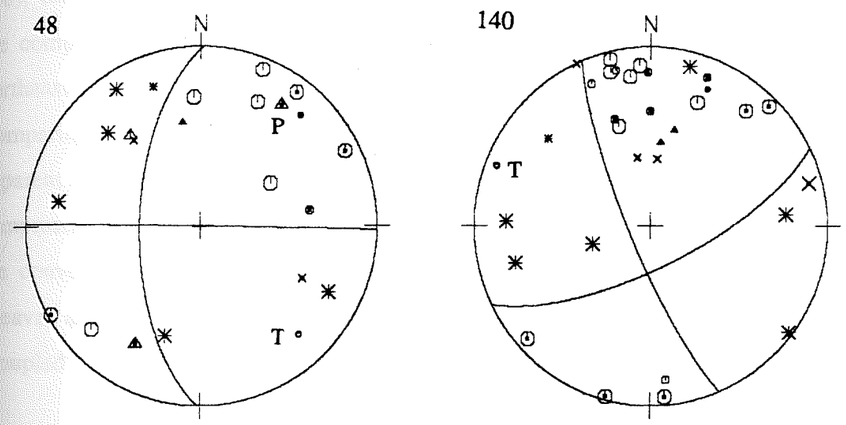

Figure 2.12. Two well constrained focal mechanisms of Mt. St. Helens earthquakes with magnitudes greater than 3.0.

event 140, which located near the south side of Cowlitz river, is rotated somewhat from northeast to north. Apart from the volcanic cone and Elk Lake areas there are five focal mechanisms of earthquakes with magnitudes equal to or greater than 2.0 (Figure 2.13). Three of them located near Cowlitz River (event 19, 112, 138), one (event 83) was below the cone and the other (event 59) was considered to be an explosion. Even though the locations were very close (event 19 and event 138), the focal mechanisms are not exactly same. For the Mt. St. Helens region the composite plots of P and T axes shows that the P axes axes tend to orient northeast-southwest and T axes tend to orient northwest-southeast (Figure 2.14). Comparing this pattern with that in shallow Puget Sound and the Cascades, the apparent compressional and tensional axes are rotated clockwise, and the apparent compressional axis in the Mt. St. Helens area is oriented closer to the direction of the convergence between the Juan de Fuca and North American plates, leading Weaver and Smith (1983) to conclude that the subduction zone is more strongly "coupled" in southwest Washington.

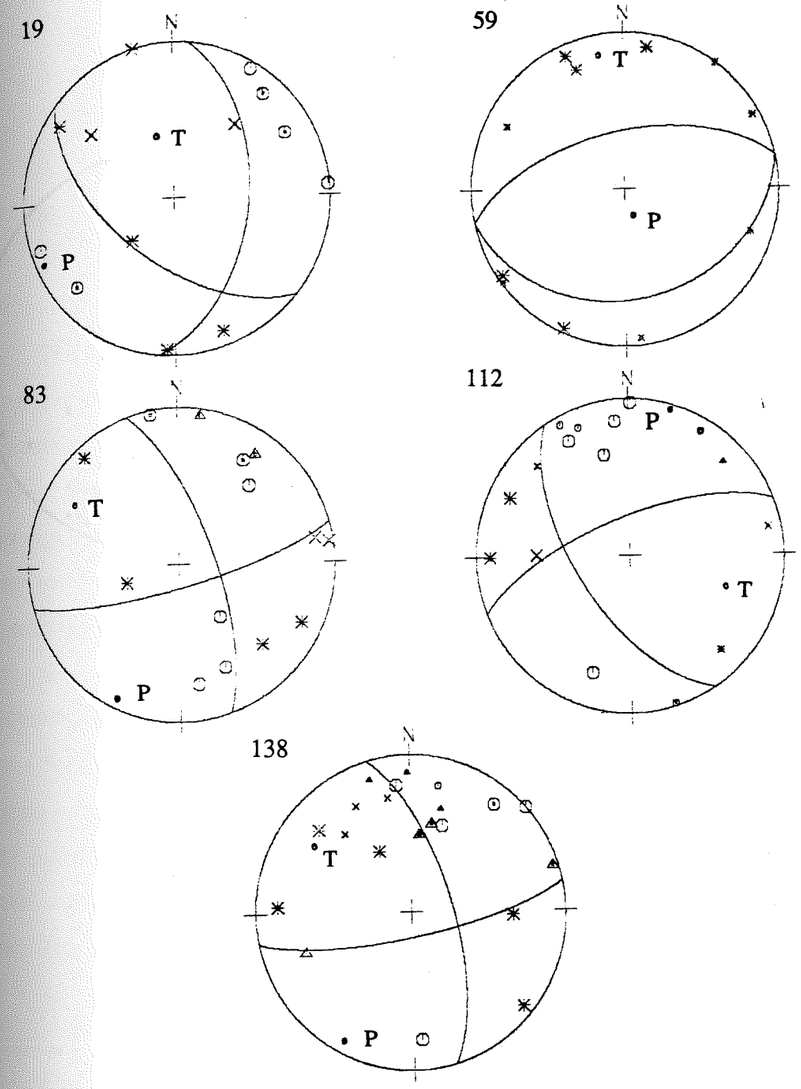

Figure 2.13. Five well constrained focal mechanisms of Mt. St. Helens earthquakes with magnitudes greater than 2.0.

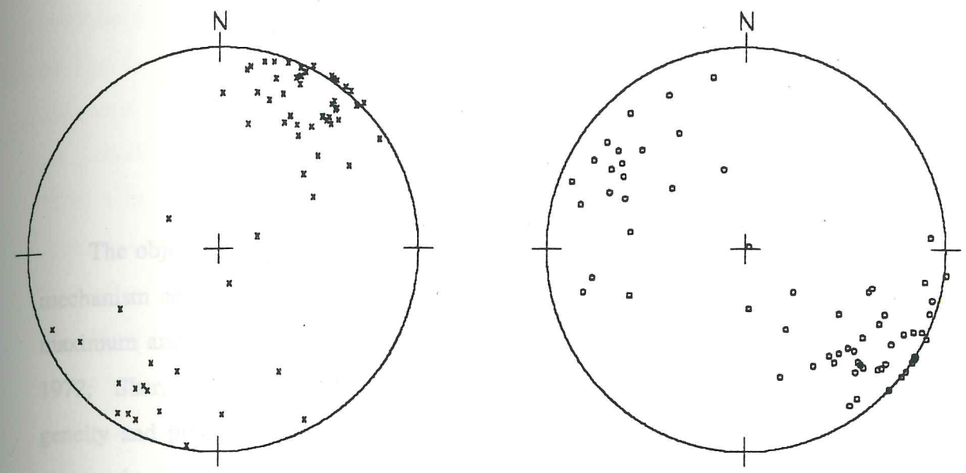

Figure 2.14. Lower-hemisphere, equal area projections of P (left) and T (right) axes from focal mechanisms of 73 Mt. St. Helens earthquakes. All crosses are P axes, and all circles are T axes.

Chapter 3

Stress Analysis - Theory and Method

The objective of this research is to deduce the regional stress state from focal mechanism solutions. Groupings of P and T axes are considered as approximate maximum and minimum compression directions in some stress analyses (Crosson, 1972; Sbar, 1983; Weaver, 1983). However, because of the crustal inhomogeneity and preexisting faults (zones of weakness), the principal stress directions are poorly constrained by individual focal mechanism solutions (Mckenzie, 1969). Under the assumption that on a weak plane, slip always occurs along the direction of the resolved shear stress in that plane, Mckenzie (1969) pointed out that compressional stress must be within 90° of the P axis in the dilatational quadrant of a focal mechanism solution. This means that one focal mechanism corresponds to an independent stress tensor family, not one set of principle stresses. Therefore an individual P axis is not always coincident with the true compressional stress axis. But the overlap of the stress families for a group of focal mechanisms may be taken as the stress range over the region (Gephart and Forsyth, 1984).

In 1974 Carey and Brunier created the first practical method to determine a regional stress tensor from a group of field measurements. Many further efforts were made to improve and apply the basic method (Angelier *et al.*, 1981a,b; Armijo *et al.*, 1982). A general definition of the inverse problem of computing the components of the regional stress tensor from geologic field data such as the measurements of the strike and dip of several faults and the directions and the

senses of relative motion along these faults was given by Angelier *et al.* (1982). To apply the inverse technique developed for stress inversion from field data to stress inversion from earthquake focal mechanisms, it is necessary to select one of the two possible nodal planes from each focal mechanism as the true fault plane (Ellsworth and Zhonghuai, 1980). If there is no additional information, for example knowledge of mapped faults, or known distribution of aftershocks, it is difficult to identify which nodal plane is the fault plane under the assumption of double-couple seismic source. The significant advantage of the method developed by Gephart and Forsyth (1984) for determining the stress tensor from focal mechanisms is that it provides an objective selection of fault plane from two nodal planes without additional tectonic or geologic information.

The basic assumption of Gephart and Forsyth method is same as that of Mekenzie's: the slip on the fault plane is in the direction of the resolved shear stress on that plane or, equivalently, that there is zero shear stress on the plane in the direction normal to the slip. In Figure 3.1 there are two sets of Cartesian coordinates, X and X' systems. The X' system is defined by fault plane geometry, x_1' is the normal of the fault plane, x_2' is the intersection of the two nodal planes, x_3' is along the slip direction. Here it is assumed that the fault plane is known. The X system is set along the orientations of three principal stresses. Then in X' system the stress tensor is written as:

$$\sigma'_{ij} = \beta_{ip}\beta_{jq}\sigma_{pq}, \tag{3.1}$$

where β_{ij} is an angle cosine between primed and unprimed coordinates. The shear stress in x_2' can be expressed by three principal stresses:

$$\sigma'_{12} = \beta_{11}\beta_{21}\sigma_1 + \beta_{12}\beta_{22}\sigma_2 + \beta_{13}\beta_{23}\sigma_3. \tag{3.2a}$$

According to the assumption, the shear stress should be zero in the direction perpendicular to x_1'. So:

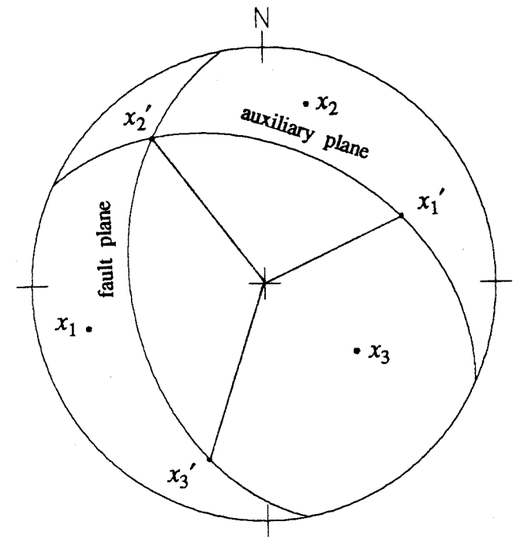

Figure 3.1. Two sets of Cartesian coordinates. X system is set along the directions of three principal stresses. X' system is defined by fault plane geometry, x_1' is in the normal of the fault plane, x_2' is the intersection of the two nodal planes, x_3' is along the slip direction.

$$\beta_{11}\beta_{21}\sigma_1 + \beta_{12}\beta_{22}\sigma_2 + \beta_{13}\beta_{23}\sigma_3 = 0. \tag{3.2b}$$

Since x_1' and x_2' are perpendicular each other, there is a relation:

$$\beta_{11}\beta_{21} + \beta_{12}\beta_{22} + \beta_{13}\beta_{23} = 0. \tag{3.3}$$

Combining (3.2b) and (3.3):

$$\frac{\sigma_2 - \sigma_1}{\sigma_3 - \sigma_1} = -\frac{\beta_{13}\beta_{23}}{\beta_{12}\beta_{22}}. \tag{3.4}$$

(3.4) is (2a) of Gephart and Forsyth (1984). The left side is a ratio dependent on the magnitudes of three principal stresses. The right side is defined as a parameter (Etchecopar *et al.*, 1981) R, such that:

$$R = -\frac{\beta_{13}\beta_{23}}{\beta_{12}\beta_{22}}. \tag{3.5}$$

If it is assumed $\sigma_1 \geq \sigma_2 \geq \sigma_3$, the value of R should be in the range $0 \leq R \leq 1$. For given fault geometry, the stress models with $R < 0$ or $R > 1$ will not generate the observed slip on that fault plane (Gephart and Forsyth, 1984). The R value is one of the limitations to the family of acceptable stress models. Another limitation is the sense of slip on the given fault plane. If the dot product of the traction and the slip vector on the upper fault block is negative, it violates the basic assumption stated before. Even though this type of stress model satisfies (3.4), it is not accepted.

A stress tensor can be uniquely determined by six independent parameters; for example, three parameters for defining principal directions, two parameters for giving magnitudes of two principal stresses and one parameter R for giving the ratio of magnitudes of three principal stresses. Knowing the stress tensor and the fault plane from a focal mechanism solution, the slip direction on that plane is predictable. Comparing the predicted slip direction with the observed slip direction on a fault plane, the angular difference between the two directions is a

measurement of misfit between the model and the observation. Figure 3.2 shows this description. Another way of viewing this situation is that a single rotational transformation of the model stress state, through an angle θ normal to the slip plane, can be made to bring the observations and model into agreement. Gephart and Forsyth (1984) however, in contrast to earlier investigators who used θ as a measure of misfit, pointed out that there may be some other axis about which a rotation by angle θ′ (where $\theta' < \theta$) will bring the model and observations into agreement. They argued convincingly that this more general rotation, reflecting possible errors in the fault plane solution, is a better measure of misfit than the angle θ confined to the fault plane. The Figure 3.3 is an attempt to depict this more general rotation angle θ′. The angle θ′ is perhaps best understood as the minimum single axis rotation necessary to bring the theoretical stress model being tested into exact agreement with the observed slip direction.

In the general case, a focal mechanism solution does not tell which nodal plane is the true fault plane unless there is additional information. For each stress model there are two minimum rotation angles, one for each of the two nodal planes. In this technique the smaller one is chosen as a measurement of the misfit, and the corresponding nodal plane is taken as the fault plane. This resolves the ambiguity of selecting a fault plane from the focal mechanism. The earlier stress inversion method only considered the error in the slip direction relative to the fixed fault plane (Angelier *et al.*, 1982). The advantage of the method of Gephart and Forsyth (1984) is that it allows for error in the orientation of fault planes as well as slip directions. If the fault plane is known, it can be taken as fixed in the method.

As shown in Figure 3.3, the fault plane geometry is rotated through an angle θ′ around an arbitrary axis in order to coincide with the geometry of the stress model. The problem is how to find the minimum rotation or how to find the

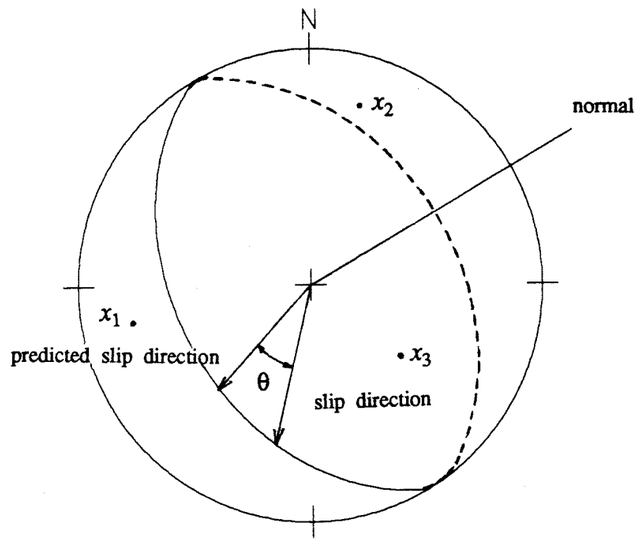

Figure 3.2. Slip direction on the fault plane from focal mechanism solution and the predicted slip direction produced by the stress tensor on the same plane. θ is the angle difference between two slip vectors.

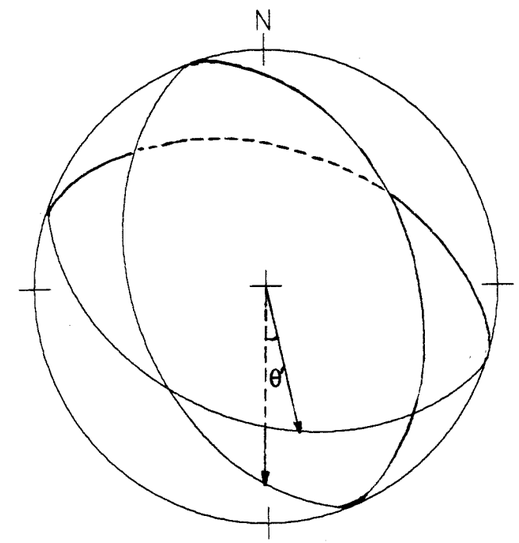

Figure 3.3. Slip direction on the fault plane from focal mechanism, and the predicted slip direction produced by the stress tensor on the other plane. θ is the angle difference between two slip vectors.

minimum rotation axis. If the relation between rotated geometry, plane B and vector x_{1b}', and principal stress is expressed by β_{ij}', then:

$$\beta'_{ij} = a_{ik}\beta_{kj}, \tag{3.6}$$

where a is a rotation matrix. The new matrix β' relates the same principal stress directions to the rotated fault plane geometry. To satisfy the geometry of a prescribed stress model requires a β' such that:

$$R = -\frac{\beta_{13}'\beta_{23}'}{\beta_{12}'\beta_{22}'}. \tag{3.7}$$

a_{ij} is a rotation matrix in (3.6). It is constructed by a rotation angle θ' and direction cosines of rotation axis, c_1, c_2, c_3 (LePichon *et al.*, 1973):

$$a = \cos\theta' \begin{bmatrix} 1 & 0 & 0 \\ 0 & 1 & 0 \\ 0 & 0 & 1 \end{bmatrix} + (1 - \cos\theta') \begin{bmatrix} c_1^2 & c_1c_2 & c_1c_3 \\ c_2c_1 & c_2^2 & c_2c_3 \\ c_3c_1 & c_3c_2 & c_3^2 \end{bmatrix}$$

$$+ \sin\theta' \begin{bmatrix} 0 & -c_3 & c_2 \\ c_3 & 0 & -c_1 \\ -c_2 & c_1 & 0 \end{bmatrix} \tag{3.8}$$

Since the determinant of a is equal to zero, if the rotation axis is specified (c_1, c_2, c_3 are known), the angle θ' will be known by solving the equation (Gephart and Forsyth, 1984):

$$A + B\sin\theta' + C\cos\theta' + D\sin\theta'\cos\theta' + E\cos^2\theta' = 0, \tag{3.9}$$

where A, B, C, D, E are constants which depend on the attitude of the rotation axis. By substituting $x = \cos\theta'$ into (3.9):

$$(A^2 - B^2) + 2(AC - BD)x + (2AE + B^2 + C^2 - D^2)x^2 \cdot$$

$$+ (CE + BD)x^3 + (D^2 + E^2)x^4 = 0 \tag{3.10}$$

The maximum real root of (3.10) gives the smallest rotation angle for a fixed

rotation axis.

To reduce the computation time, one of the three x' axes (see Figure 3.1) is taken to be a starting point depending on which of them requires the smallest rotation to acquire the geometry fitting (3.7). Analytical expressions for the minimum rotations about three x' axes in terms of R and β_{ij} are given by Gephart and Forsyth (1984). Then by computing the amount of rotation around two other axes which are near the starting axis, the slope about the starting point is determined. In the downslope direction, a new axis is selected and the steps above repeated until the procedure converges on the absolute minimum rotation. This absolute minimum rotation will be taken as the misfit between model and the observation. Solving a fourth order polynomial requires lengthy computation. For this reason Gephart and Forsyth (1984) generated an approximate method by assuming that the smallest of the rotations about the three x' axes is approximately equal to the absolute minimum rotation needed to match the stress model. The amount of rotation around each x' axis is calculated by the analytical expression (see table 3.1). In this way tedious calculation is avoided.

An appropriate normative measure of misfit is needed for minimizing the residuals for all observations. In many inverse problems minimizing the sum of the squares of the misfit or least squares minimization is commonly used (least-squares). However, in some cases least-squares minimization may place too much emphasis on the extreme data (Claerbout and Muir, 1973). And one-normal measure of misfit is suggested to be better than two-normal measure of misfit (Gephart and Forsyth, 1984).

In the procedure of finding the best-fitting model, the method of grid search is adopted. Setting one stress model, three principal directions and one R value, the one-normal misfits between this model and all observations are summed:

$$S = \sum_{i=1}^{i=n} |\theta_i'| \tag{3.11}$$

Table 3.1. Analytical Expression for θ (Gephart and Forsyth, 1984)

Table 3.1

Rotation Axis	Algorithm	Period
x_1'	$\theta = \tan^{-1}\left(\frac{\beta_{13}\beta_{23} + R\beta_{12}\beta_{22}}{R\beta_{12}\beta_{32} + \beta_{13}\beta_{33}}\right)$	π
x_2'	$\theta = \tan^{-1}\left(\frac{\beta_{13}\beta_{23} + R\beta_{12}\beta_{22}}{R\beta_{22}\beta_{32} + \beta_{23}\beta_{33}}\right)$	π
x_3'	$\theta = \cos^{-1}\left(\left[0.5 \pm \left(0.25 - \frac{1}{(4 + k^2)} \right)^{\frac{1}{2}} \right]^{\frac{1}{2}} \right)$ $k = \frac{R\beta_{12}^2 + \beta_{13}^2 - R\beta_{22}^2 - \beta_{23}^2}{R\beta_{12}\beta_{22} + \beta_{13}\beta_{23}}$	$\frac{\pi}{2}$

Tabel 3.2. Relation Between R and α

Table 3.2

α	R
2,000	0.999
19	0.9
3.0	0.5
1.5	0.2
1.001	0.0005

For each stress model a single S value represents the fit of the model to all the data. The model with the minimum S value is chosen to be the best-fitting model.

In the work of Mckenzie (1969), he cited the value of α to express the relationship of the magnitude of three principal stress. α was defined as:

$$\alpha = \frac{2\sigma_1 - \sigma_3 - \sigma_2}{\sigma_2} - \sigma_3$$

For a given focal mechanism with known fault plane, corresponding various α value the orientation of the greatest principal stress will vary in different regions. The relation between α and R can be derived very quickly from (3.4), (3.5) and the definition of α:

$$R = \frac{\alpha - 1}{\alpha + 1}$$

The R values corresponding to the α values are given in Table 3.2. Using the method of Gephart and Forsyth (1984), the various areas in which the greatest principal stress lies depending on different α values (Mckenzie, 1969) can be recreated as a confirmation of the analysis method. A pure strike-slip focal mechanism shown in Figure 3.4 is chosen to be tested. Figure 3.5 is the stress grid, each cross mark expresses one direction of σ_1, the greatest principle stress which has 20 pairs of σ_2 and σ_3 on the plane perpendicular to σ_1. Here we assume that the fault plane is known. For one focal mechanism, the model with zero misfit is taken as the best-fitting model. As discussed above, the approximate method will miss some models which have zero misfit as a result of the grid search method. Figure 3.6 gives the test results for various R values if the the horizontal plane is assumed as the fault plane of the focal mechanism in Figure 3.4. The shapes of the regions covered by possible maximum principle stresses are almost identical to the theoretical results of Mckenzie (Figure 3.7). If we assume the vertical plane as fault plane, the patterns for corresponding R values

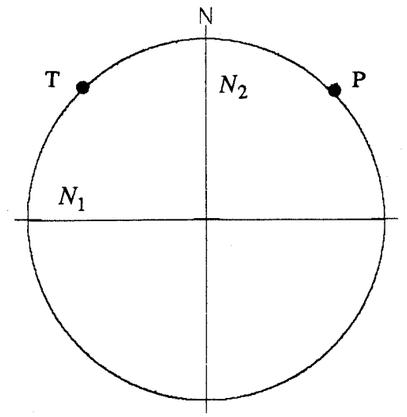

Figure 3.4. Pure strike-slip focal mechanism used to test the method.

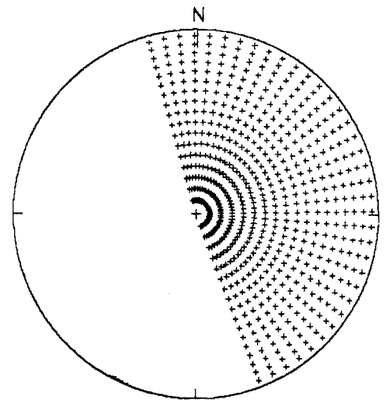

Figure 3.5. Stress grid used in the test. Each cross is one direction of σ_1. For each σ_1 there are twenty sets of σ_2 and σ_3 on the plane perpendicular to σ_1.

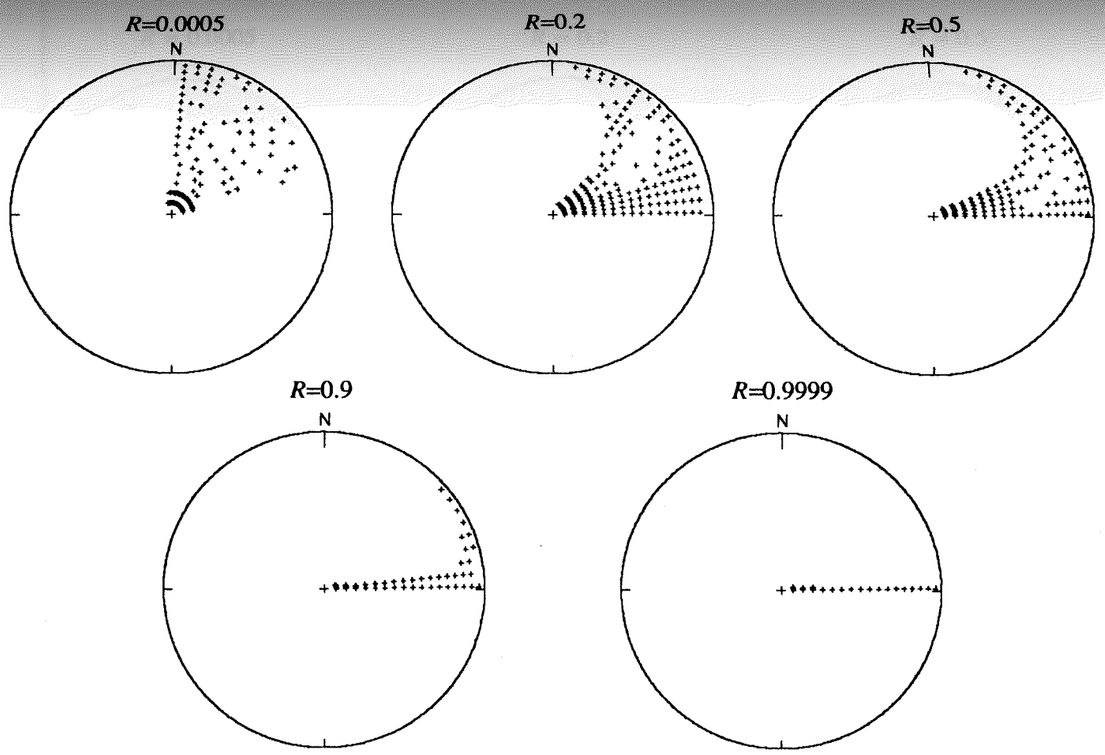

Figure 3.6. For various R values the possible orientations of σ_1 which can produce the focal mechanism in Figure 3.4 if plane N_1 is chosen as fault plane.

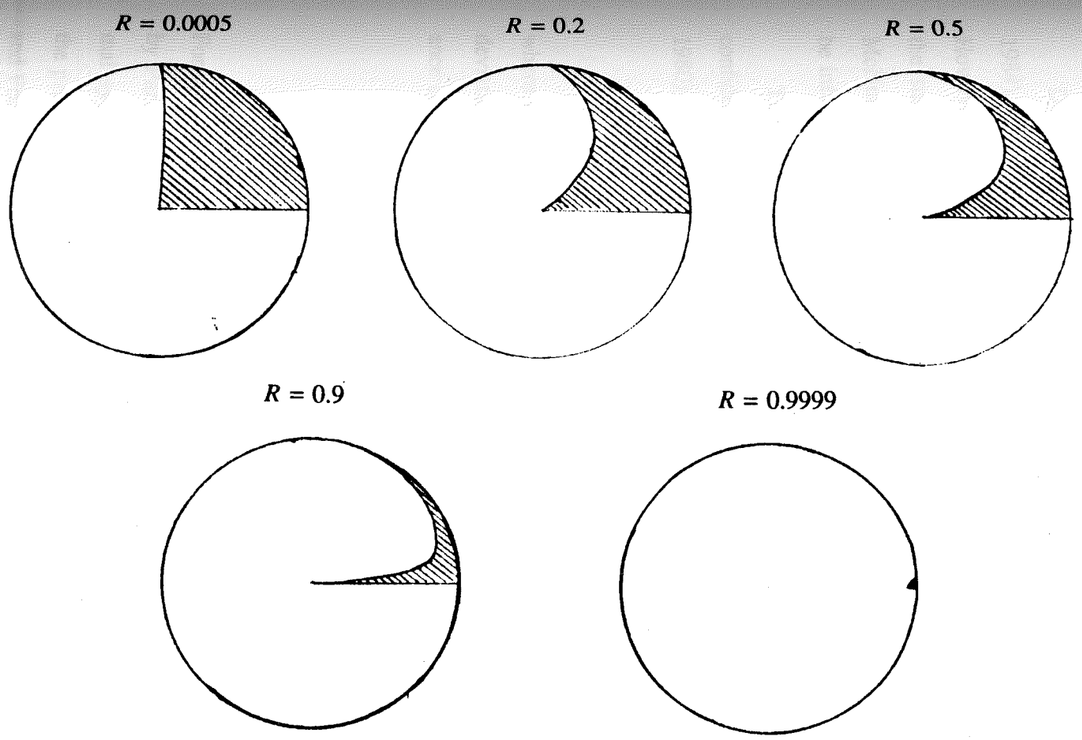

Figure 3.7. For various R values the regions of possible σ_1 for the focal mechanism in Figure 3.1 from the theoretical calculation (Mckenzie, 1969).

are absolutely symmetric (Figure 3.8).

Due to the nonnormality of the misfit distribution (Gephart and Forsyth, 1984), the confidence limit constructed for the best-fitting model is not accurate. However, if the misfit is assumed to be an independent normal random variable, the statistical method for the one-norm misfit measure developed by Parker and McNutt (1980) can be applied here. In fact, when the size of data base tends to be infinity, the normal approximation should be correct.

The misfit sum for the best-fitting model is S_{mini}. In order to determine the confidence limit, another random variable is examined first (Parker and McNutt, 1980):

$$m = \sum_{i=1}^{i=n} \frac{|\theta_i'|}{\sigma_i} \tag{3.12}$$

where θ_i' is an independent normal random variable with zero mean and standard deviations σ_i. According to Parker and McNutt, the expected value and the variance of random variable m are:

$$\overline{m} = E[m] = \left(\frac{2}{\pi}\right)^{\frac{1}{2}} n \tag{3.13}$$

$$\sigma_m^2 = E\left[(m - \overline{m})^2\right] = \left(1 - \frac{2}{\pi}\right) n \tag{3.14}$$

For small values of n, the probabilities of $m \geq M$ by chance are given in a table by Parker and McNutt (1980). In the case of large value of n ($n > 10$), the normal approximation is usually accurate enough (Parker and McNutt, 1980). When the probability is 0.05 ($\alpha = 0.05$) the value of m at the 95% limit is then (Gephart and Forsyth, 1984):

$$M_{95} = 1.96\ \sigma_m + \overline{m} \tag{3.15}$$

On the other hand, the estimate value of σ (σ_{est}) can be expressed by S_{mini} and $\overline{m}$:

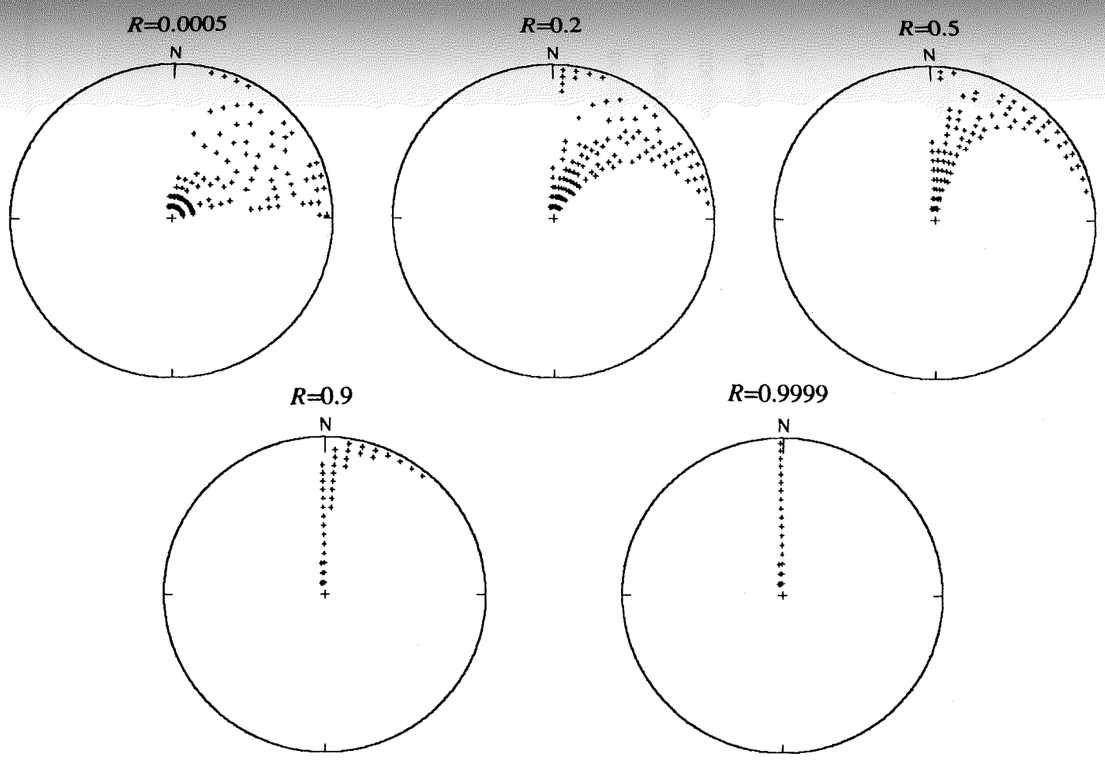

Figure 3.8. For various R values the possible orientations of σ_1 which can produce the focal mechanism in Figure 3.4 if plane N_2 is chosen as fault plane.

$$\sigma_{est} = \frac{S_{mini}}{(\frac{2}{\pi})^{\frac{1}{2}}(n-k)} \tag{3.16}$$

where k is the number of variables in the model. Then 95% confidence limit for S is constructed as:

$$S_{95} = (\frac{1.96(\frac{\pi}{2}-1)^{\frac{1}{2}}n^{\frac{1}{2}}+n}{n-k})S_{mini}. \tag{3.17}$$

Using equation (3.17) we can construct the equal misfit curves for different confidence limits and give an evaluation for the best-fitting model. The 95% confidence limit means there is only 0.05 probability that the best-fitting model could fall outside of the contour by chance.

Chapter 4

Stress Analysis - Results for Western Washington

Before undertaking the inversion a proper stress grid has to be established for searching for the model which best fits all focal mechanism solutions. Gephart and Forsyth (1984) found that the preferred σ_1 direction determined using a preliminary search with a coarse stress grid and the approximate method was in good general agreement with the alignment of P axes. Using this observation, σ_1 directions on the stress grid were set in the range which agreed with the general direction of P axes.

Because of the similarity of the composite plots of P and T axes from focal mechanisms of shallow Puget Sound and shallow Cascades earthquakes (Figure 2.9 and Figure 2.10), these two groups of focal mechanisms were combined for the analysis. This combined region will be called "shallow Puget Sound". From the distribution of P axes on the focal sphere, the azimuth of σ_1 in the stress grid was set from northwest (N60°W) to northeast (N60°E) and from southeast (S57°E) to southwest (S63°W). Similarly the plunge was set from 1° to 51°. The angular distance between grid points for σ_1 is 5° for both azimuth and plunge. Corresponding to each σ_1 direction there are twenty pairs of orthogonal σ_2 and σ_3 axes lying on the plane which is perpendicular to σ_1 direction. The angular distance of grid points for σ_2 and σ_3 successive sets of axes is 9°. In all, there are 11,000 stress models used in grid searching. The approximate method described in chapter 2 was applied in a preliminary search. For each focal mechanism one of the apparent stress axes (P, T or B), which makes a minimum misfit between model and datum, will be taken as the rotation axis.

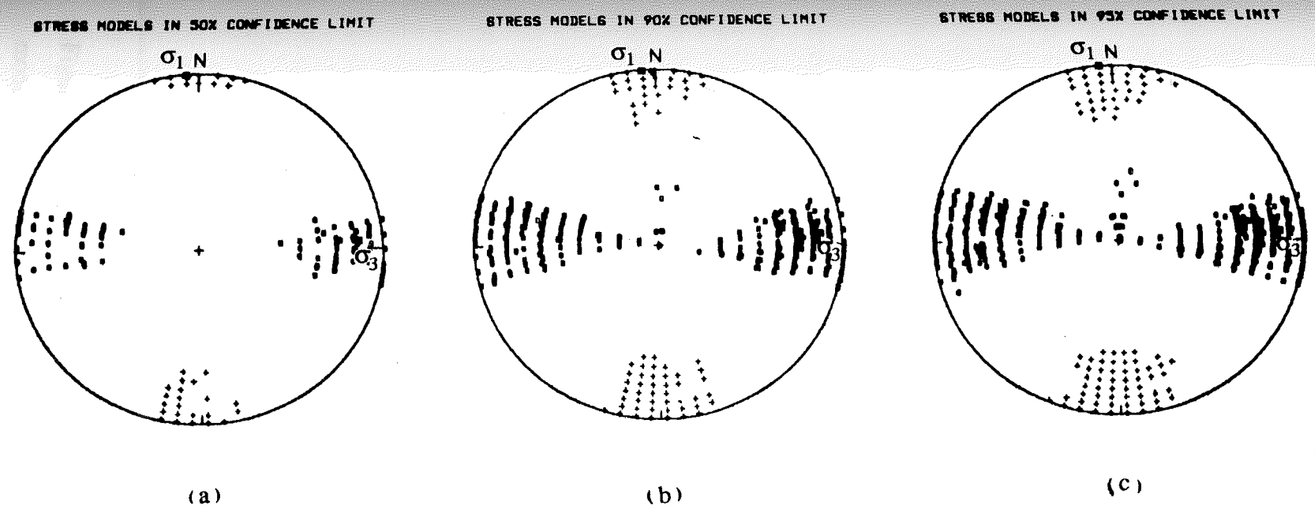

(a) (b) (c)

Figure 4.1. Results of stress inversion for seventy-six shallow Puget Sound earthquakes using Gephart and Forsyth's approximate method. The best-fitting model found in grid searching is $\sigma_1 = 1°, 356°$; $\sigma_2 = 72°, 262°$; $\sigma_3 = 18°, 86°$; $R = 0.6$. (a) 50% confidence limit; (b) 90% confidence limit; (c) 95% confidence limit.

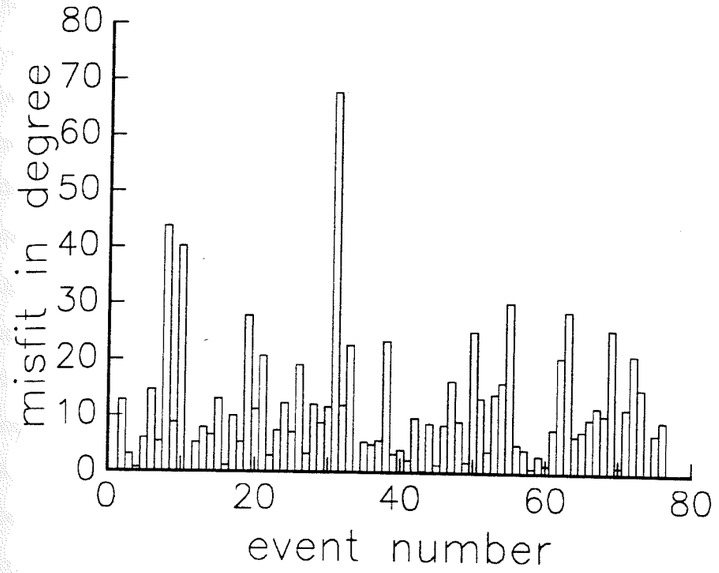

Figure 4.2. The misfit between each focal mechanism and the best-fitting model for seventy-six shallow Puget Sound earthquakes.

The single best-fitting model for seventy-six focal mechanisms in shallow Puget Sound is (plunge and azimuth) σ_1 = 1°, 356°; σ_2 = 72°, 262°; σ_3 =18°, 86°. The value of R is 0.6, and the average misfit between the model and the individual focal mechanisms is about 12.6°. Figure 4.1 shows the stress models (σ_1 and σ_3) for three different confidence limits. It is obvious that the best fit direction of σ_1 is near horizontal and oriented north-south for this group of focal mechanisms. The distribution patterns of σ_1 and σ_3 in 50%, 90% and 95% confidence limits are thus similar to those of the P and T axes (see Figure 2.9 and Figure 2.10).

Based on the preliminary result, I used the exact method on a small number of the stress models within the 50% confidence limit. The best-fitting model found using the exact method is the same as determined with the approximate method, but as is expect the average misfit is only 11.2° which is smaller than that found using the approximate method. Figure 4.2 shows the distribution of misfit for the best-fitting model. Only twelve values of misfits exceed 20°.

To test the stability of the best-fitting model to outlier data, the approximate searching procedure was repeated by deleting the focal mechanisms with misfit greater than 20°. If only one focal mechanism was deleted at a time, the best-fitting model was the same as the original one. This means the contribution of any one focal mechanism does not have a large effect on the result. If all focal mechanisms with misfit greater than 20° were deleted simultaneously, the best-fitting model still deviated only slightly from the original one, yielding σ_1 = 6°, 1°; σ_2 = 62°, 102°; σ_3 = 27°, 267°; R = 0.5.

The value of R is determined by the relative magnitudes of the three principle stresses. From the definition of R (Chapter 3), a value of 0.5 means that σ_2 lies midway between σ_1 and σ_3. Various confidence limits shown in Figure 4.1 present ranges of acceptable stress directions for different confidence levels derived from inversion of the "shallow Puget Sound" earthquakes. It indicates that

a model with north-south compression, east-west tension and an intermediate stress axis near vertical found under the hypothesis of uniform stress field (R value and the orientation do not change in the whole region) fits these focal mechanism data. Such a stress tensor agrees with the inference of many authors (Crosson, 1972; Sbar, 1983; Rogers, 1979; Molone, *et al.*, 1975; Crosson and Yelin, 1982; Yelin, 1982; Crosson and Frank, 1975; Crosson and Lin, 1975) about the stress state in the crust of western Washington.

However, the composite plot of P axes from focal mechanism in the Mt. St. Helens region and south-western Washington (Figure 2.11 and Figure 2.14) present a problem in the interpretation of the stress in western Washington. The orientation of the apparent compressional axis is approximately northeast in disagreement with adjacent regions, and if it is taken as the direction of maximum principal stress, it can be argued that plate coupling may vary along the Cascadia subduction zone (Weaver and Smith, 1983).

I performed stress inversion using seventy-three well constrained focal mechanisms of earthquakes in the Mt. St. Helens region (the distribution of these earthquakes are shown in Figure 2.11) with the approximate method and the same stress grid described above. The best-fitting model found for St. Helens earthquakes is $\sigma_1 = 1°, 6°$; $\sigma_2 = 81°, 269°$; $\sigma_3 = 9°, 96°$ and $R = 0.4$. The average misfit is 12.7°. Figure 4.3 shows the stress models in 50%, 90% and 95% confidence limits. Note that the ranges of acceptable stress directions are quite narrow for various confidence levels. The confidence limits were constructed by the equal misfit contours in a four parameter space. The value of misfit for each contour was calculated from equation 3.17. Relatively fewer models in various confidence limits implies that the misfit value found for the best-fitting model is much less than that found for other models.

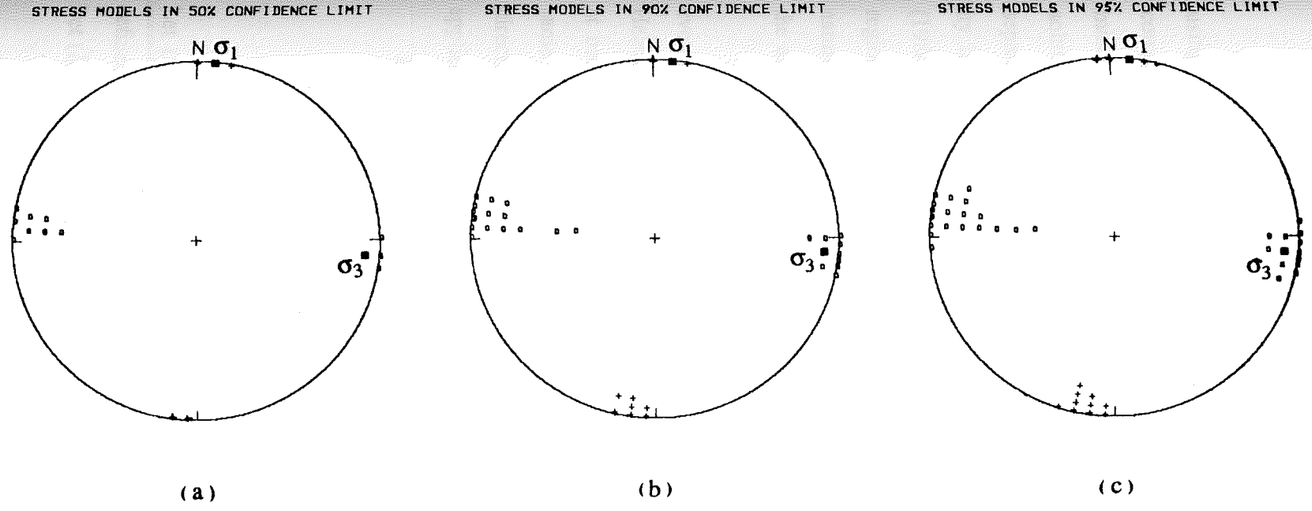

(a) (b) (c)

Figure 4.3. Results of stress inversion for seventy-three Mt. St. Helens earthquakes using Gephart and Forsyth's approximate method. The best-fitting model found in grid searching is $\sigma_1 = 1°, 6°$; $\sigma_2 = 81°, 269°$; $\sigma_3 = 9°, 96°$; $R = 0.4$. (a) 50% confidence limit; (b) 90% confidence limit; (c) 95% confidence limit.

For the Mt. St.. Helens region, the average misfit for the best-fitting model using the exact method is 10.1° (the misfit distribution is shown in Figure 4.4) comparable to the shallow Puget Sound results. Only six focal mechanisms have misfit larger that 20°. To ensure that these large misfits were not distorting the solutions, they were individually and collectively removed from the data set while separate inversions were performed. The results of this experiment yielded stability in the principal axis directions to within a few degrees. Gephart and Forsyth (1984) have noted that if R is allowed to vary from place to place within the region, the degree of misfit will be reduced. This may correspond to the case in nature given large scale inhomogeneity. Thus the misfit that we computed under the assumption of uniform R should be an up bound.

The 95% confidence regions of the two sets of principal axis directions (and even the more restricted 50% confidence regions) for shallow Puget Sound and St. Helens regions overlap. The angular separation of the two sets of axes differ by at most about 10°. The two sets of best-fitting axes are plotted together on the same focal hemisphere in Figure 4.5. To further compare the mean P and T axis directions with the results of the stress inversion, spherical statistics can be applied.

From azimuth (az) and plunge (pl), the direction cosines can be written as:

$$l = cos(pl)cos(az) \tag{4.1}$$

$$m = cos(pl)sin(az) \tag{4.2}$$

$$n = sin(pl). \tag{4.3}$$

Let (l_i, m_i, n_i), $i = 1,...,n$ be n direction cosines, the spherical mean direction was defined as the direction of the resultant of (l_i, m_i, n_i), $i = 1,...,n$ (Mardia, 1972). Let $(\overline{l_0}, \overline{m_0}, \overline{n_0})$ be the direction cosines of the resultant, then:

$$\overline{l_0} = \sum_{i=0}^{n} \frac{l_i}{L} \tag{4.4}$$

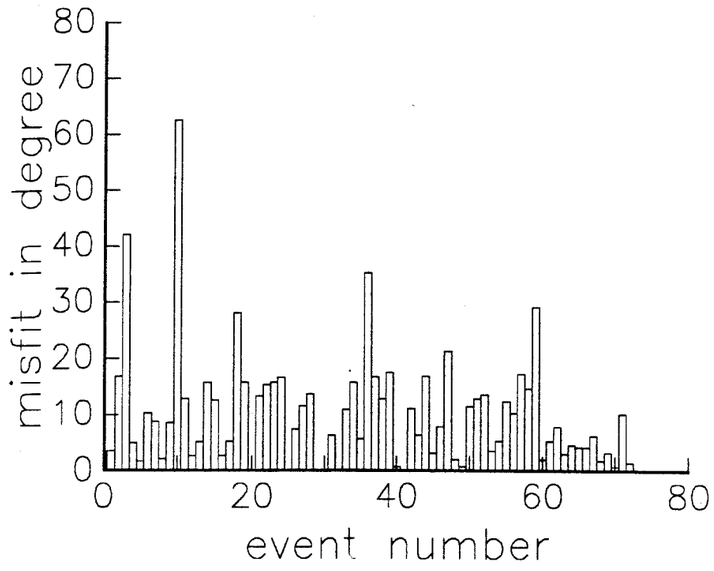

Figure 4.4. The misfit between each focal mechanism and the best-fitting model for seventy-three St. Helens earthquakes.

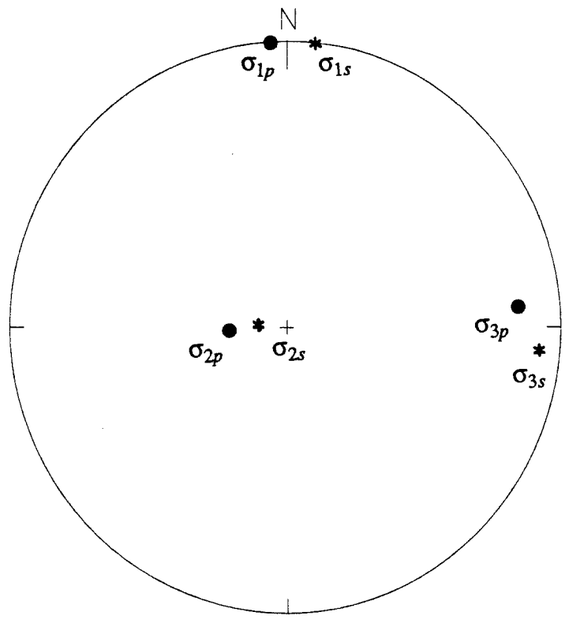

Figure 4.5. Comparison between the best-fitting models for shallow Puget Sound and Mt. St. Helens. The model with subscript *s* is for Mt. St. Helens, and the model with subscript *p* is for shallow Puget Sound.

$$\overline{m}_0 = \sum_{i=0}^{n} \frac{m_i}{L} \tag{4.5}$$

$$\overline{n}_0 = \sum_{i=0}^{n} \frac{n_i}{L}. \tag{4.6}$$

where L is the length of the resultant given by:

$$L = [(\sum l_i)^2 + (\sum m_i)^2 + (\sum n_i)^2]^{\frac{1}{2}}. \tag{4.7}$$

L will be as large as n if the observations are clustered about a direction whereas if the observations are very dispersed such as in the uniform case, L will be small. Hence L is a measure of concentration about the mean direction if it exists (Mardia, 1972). The spherical variance is defined as

$$S^* = \frac{(n - L)}{n}, \qquad 0 \le L \le n, \ 0 < S^* < 1. \tag{4.8}$$

The mean directions of P axes for shallow Puget Sound and Mt. St. Helens region were calculated separately. Because P axes cluster in two regions on the focal sphere (Figure 2.9, Figure 2.10 and Figure 2.14), two mean directions were calculated, one on the northern-hemisphere and the other on the southern-hemisphere. For shallow Puget Sound thirty-six P axes lie in the northern-hemisphere. The mean direction is: $az = 4°$, $pl = 11°$; the length of the resultant is $L = 32.2$ and the spherical variance is $S = 0.107$. Forty P axes lie in the southern-hemisphere. The mean direction is: $az = 181°$,$pl = 15°$; $L = 36.4$ and $S = 0.089$. Comparing with σ_1 of the best-fitting model in Figure 4.6, the azimuth is still north-south, but the plunge changes about 10°. There is no remarkable difference. In the Mount St. Helens area, fifty-five P axes lie on the northern-hemisphere. The mean direction is $az = 31°$, $pl = 15°$; $L = 50.9$ and $S = 0.074$. Eighteen P axes lie in the southern-hemisphere. The mean direction is $az = 208°$, $pl = 22°$; $L = 15.8$ and $S = 0.121$. It is obvious that the mean direction of P axes

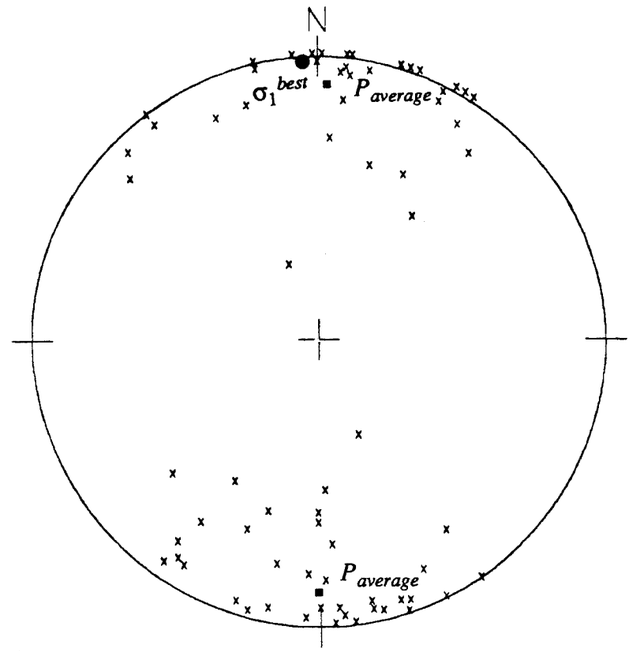

Figure 4.6. Comparison between σ_1 direction of the best-fitting model and the average directions of all P axes for shallow Puget Sound earthquakes.

differs from the σ_1 direction of the best-fitting model for St. Helens (Figure 4.7). The mean direction of P axes seems to be northeast-southwest while σ_1 of the best-fitting model orients north-south. Therefore, if P axis of focal mechanisms can be taken approximately as the maximum compressional axis, in the sense of mean direction, we can say there is a discrepancy between the directions of compressional axes in the "shallow Puget Sound" and the Mt. St. Helens regions. On the other hand, the best-fitting models found for these two regions on the premise that P axes need not be identical to the maximum compressional axis for the region show nearly identical stress states for these two regions. Because the basic idea of the method produced by Gephart and Forsyth (1984) is to find the overlap of all stress families which can initiate a correct sense of slip on each nodal plane, and the method itself involves the consideration of the difference between P axis and the true compressional axis, choosing the best-fitting model found in grid searching to be the stress tensor of the region is more objective than simply picking the mean direction of P axes as maximum compressional axis.

In initially applying the stress inversion method, the magnitude of the earthquakes was not considered as a possible controlling factor. However, it may be argued that higher magnitude earthquakes may carry more information of the regional stress field while lower magnitude earthquakes reflect more local stress state. Among all shallow focal mechanisms (including shallow Puget Sound and Mt. St. Helens events) seventeen have magnitudes greater than or equal to 3.0 with two of these events in St. Helens area. The stress inversion was performed on the fifteen events in "shallow Puget Sound" data set to see if significantly different results emerged. The best-fitting model for this inversion is: $\sigma_1 = 6°, 356°$, $\sigma_2 = 71°, 103°$, $\sigma_3 = 18°, 264°$, in good agreement with our previous results. Consequently, it can be inferred that magnitude does not have an important influence on the results obtained from stress inversion.

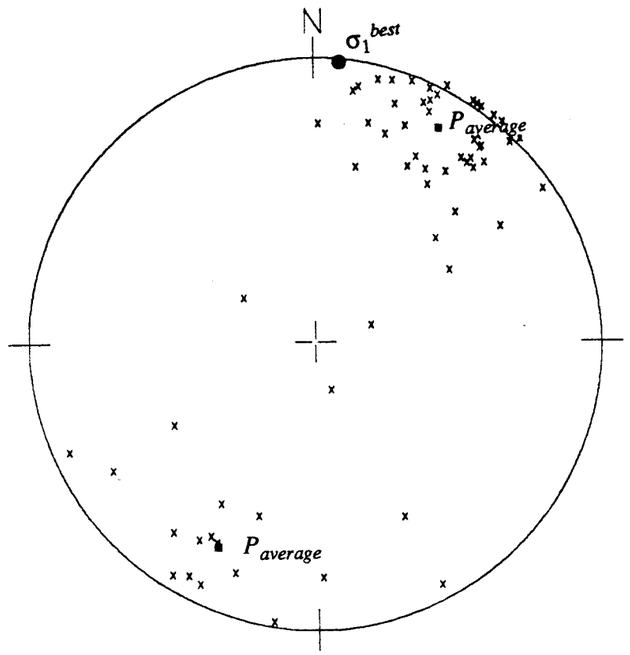

Figure 4.7. Comparison between σ_1 direction of the best-fitting model and the average directions of all P axes for Mt. St. Helens earthquakes.

If the hypothesis of slip on preexisting faults is correct within the subducted Juan de Fuca slabs, we can try the same method to investigate the stress state there. The composite plots of P and T axes from focal mechanisms of deep earthquakes in Puget Sound (Figure 2.7) does not present a cluster distribution of P and T axes. Thus it was necessary to use a stress grid with σ_1 directions covering whole focal sphere. The choice of σ_2 and σ_3 was the same as before.

Figure 4.8 displays the searching result from forty-one subcrustal focal mechanisms. The best-fitting model is $\sigma_1 = 51°, 245°$; $\sigma_2 = 26°, 13°$; $\sigma_3 = 26°, 117°$ and $R = 0.1$. The minimum compression or the tension axis is in E27°S. The azimuth of the maximum compression axis is oriented southwest. The value of R means that the magnitude of intermediate stress is close to that of the maximum principle stress. Perhaps more significant is the fact that the minimum principal stress is significantly less than the other two, indicating that physical processes such as slab sinking may control this stress. All possible σ_1 axes cluster near the center of the focal sphere. This is a significant difference from the result for shallow Puget Sound (see Figure 4.1). The 95% confidence limit shows that all acceptable σ_3 could be in any direction. The relative motion of the plates indicates that the Juan de Fuca plate convergences with the North American plate in NE direction (Atwater, 1970). The maximum compression of the best-fitting model has an azimuth in the direction of plate convergence. This differs from the previous analysis of stress which only depended on P axes (Taber, 1985), in that σ_1 is normal to the subducting plate.

The misfit between each focal mechanism and the best-fitting model is presented in Figure 4.9. The average misfit from exact method is 14.5°. Compared with the average misfit found for shallow Puget Sound and Mt. St. Helens, the magnitude of average misfit is higher, possibly reflecting stress inhomogeneity within the slab.

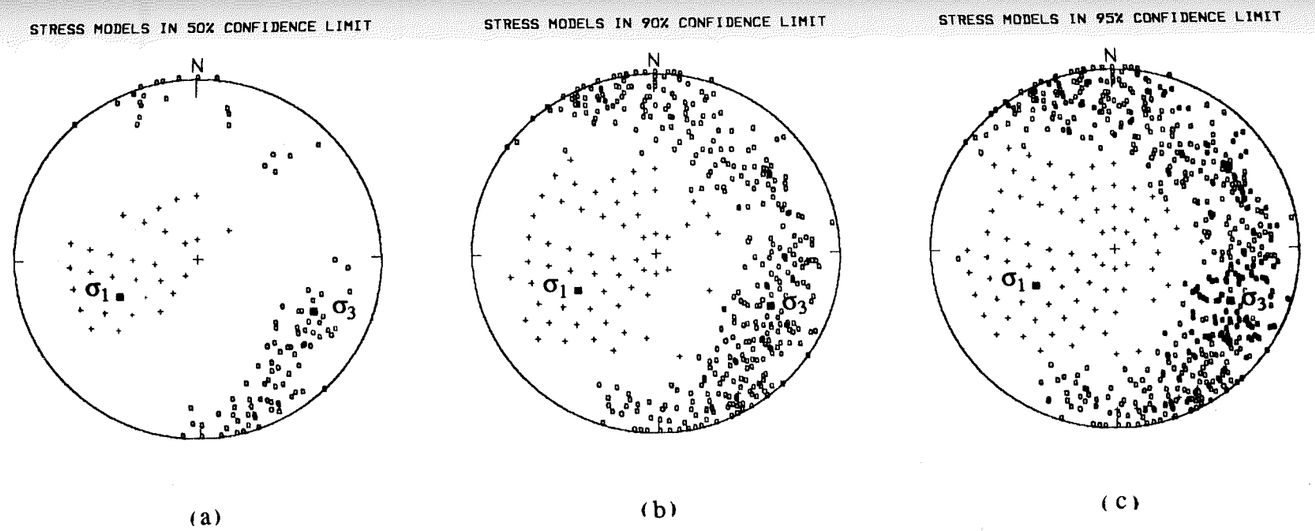

Figure 4.8. Results of stress inversion for subcrustal earthquakes using Gephart and Forsyth's approximate method. The best-fitting model found in grid searching is $\sigma_1 = 51°, 245°$; $\sigma_2 = 26°, 13°$; $\sigma_3 = 26°, 117°$; $R = 0.1$. (a) 50% confidence limit; (b) 90% confidence limit; (c) 95% confidence limit.

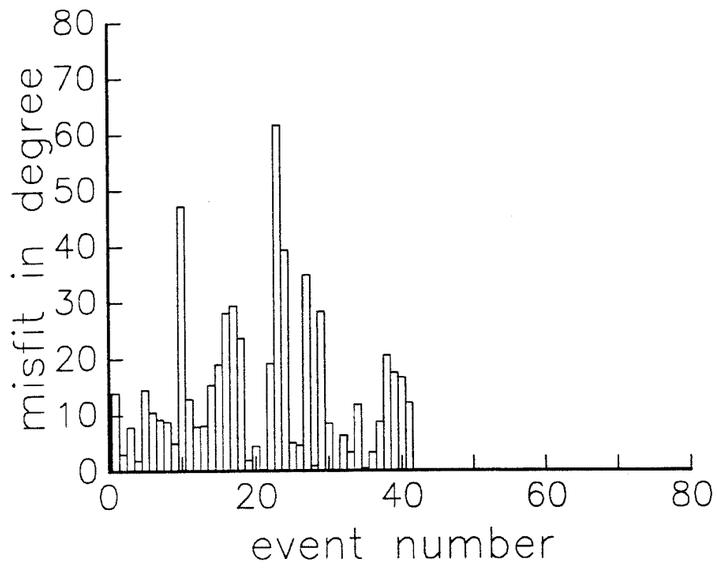

Figure 4.9. The misfit between each focal mechanism and the best-fitting model for forty-one Puget Sound subcrustal earthquakes.

Chapter 5

Discussion

The principal stress directions of the best-fitting models found in this stress inversion for shallow Puget Sound and Mt. St. Helens confirms NS horizontal compression in the crust of western Washington first suggested by Crosson (1972). The results of this study indicate that there is no significant change in stress orientation between the Puget Sound region and the Mt. St. Helens region in contradiction to the interpretation of Weaver and Smith (1984). The results thus agree against any change in stress coupling across the Cascadia subduction zone. In fact NS compression is the dominant tectonic characteristic along the west coast of United States (Zoback and Zoback, 1980; Sbar, 1981). Because of the rather limited extent of the Juan de Fuca plate in relationship to the extensive San Andreas and Fairweather right lateral transform fault systems which form most of the remainder of the western plate boundary of North America, the stress state of the crust in western Washington may be controlled more by the large scale transform motion between the Pacific and North American plates (Zoback and Zoback, 1980).

The accumulation of tectonic strain (Savage *et al.*, 1981) may be thought to be at various with the NS compression interpreted from the focal mechanism analysis. It is important however to note that the strain rate is very low (< 0.02 μ strain/yr) (Lisowski, *et al.*, 1988) and that strain measurements reflect only incremental changes in stress whereas focal mechanisms likely reflect the large scale regional ambient stress. It is also not clear whether geodetic strain measurements reflect elastic or inelastic deformation. Thus these two sets of interpretations may

not be in conflict.

When Gephart and Forsyth (1984) applied the stress inversion method to the San Fernando Earthquake Sequence, they found that the main shock fit the best stress model rather poorly. One possibility is that the main shock perturbed the stresses in the region such that the stresses associated with the main shock were somewhat different from those felt by the after-shocks (Gephart and Forsyth, 1984). The Elk Lake earthquake (m_b = 5.5), the largest event in western Washington since 1965 Seattle earthquake (Grant *et al.*, 1981), occurred prior to the events analyzed here and the possible perturbation that this earthquake caused in the stress field, if any, is not clear.

The stress state in the slab appears to be complicated. It is likely that no single stress state exists within the slab, so a fundamental contradiction of the hypothesis of Gephart and Forsyth's method may exist. This could explain the wide scatter results. Viewing the focal mechanism solutions (Figure 2.7), it is difficult to even estimate the directions of apparent compression and tension. But there are two remarkable characteristics: first, few low dip angle P axes are in NS direction; second, most T axes orient northeast or southeast with low dip angles. The difference between P and T axes from focal mechanisms in the crust (Figure 2.9 and Figure 2.10) and from those in the subcrust (Figure 2.7) presents convincing evidence that focal mechanism solutions contradict the suggested strong coupling between Juan de Fuca plate and North American plate (Heaton and Kanamori, 1984), at least in the regions where these intreplate earthquakes occur.

The best-fitting model found for slab earthquakes shows a general down-dip tension which could be one feature of the stress state in the subducting Juan de Fuca plate. The variety of the directions of tensional axes in different parts of the slab might be due to the superposition of down-dip tension and tension or compression in an arched plate. To test these ideas, several plots were

constructed. Figure 5.1 is a north-south cross section, along $B - B'$ in Figure 2.3. The curves shown on the cross-section represent slab contours at different longitudes from Crosson and Owens (1987). Most T axes tend to be in the slab with directions along the arch or in down-dip. A few are at angles to the slab. For the higher magnitude events, this tendency is more obvious. Figure 5.2 was plotted for eight earthquakes with magnitudes equal to or greater than 3.0. Five T axes are along the arched slab, one in the down-dip direction and the other two are at angles to the slab. The arching of the slab could result in the tension on the side of the bulge, and the pulling of the gravity might cause the tension in down-dip direction. Therefore, the complicated stress pattern is the total effect of superposition of various sources.

The configuration for P axes is quite different (Figure 5.3). Most P axes are at angles to the slab. It could be suggested that the maximum compression tends to perpendicular to the slab. However, examining the higher magnitude events (Figure 5.4), three of them have P axes in the slab with down-dip directions.

It is difficult to give a comprehensive interpretation to the deep focal mechanisms based on the present knowledge of plate geometry. The subduction environment, the temperature of the slab and the thickness could affect the stress distribution. As a result of the arching, stress may be affected by local bending. Considering all these factors, a unique stress field can not be expected in the subducting plate. Although we have taken a first step, full construction of three-dimensional mechanical and thermal models of the slab may be necessary to give a more complete understanding of the stress state and focal mechanisms generated within the subducting Juan de Fuca slab.

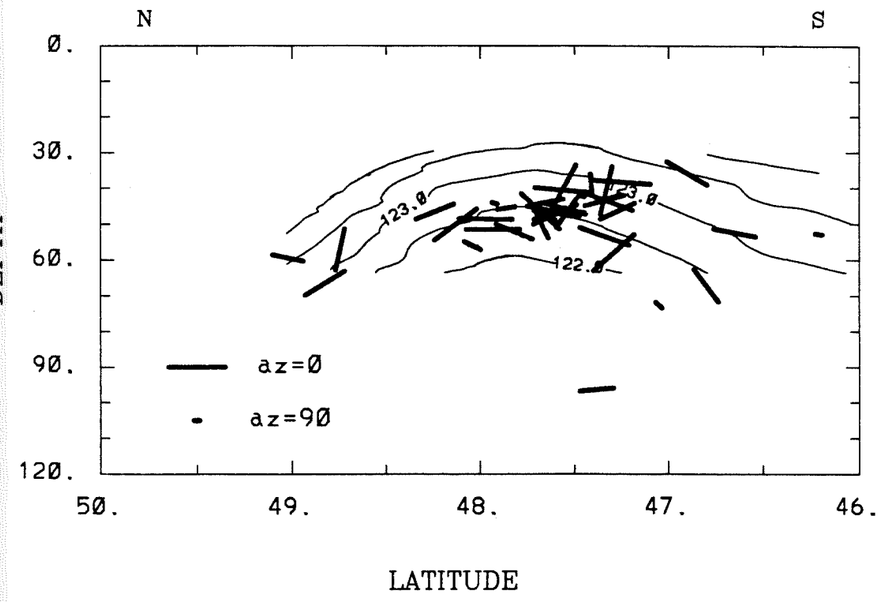

Figure 5.1. T axes of the slab earthquakes plotted in a north-south cross-section. Contours are equal longitude curves representing the arched slab.

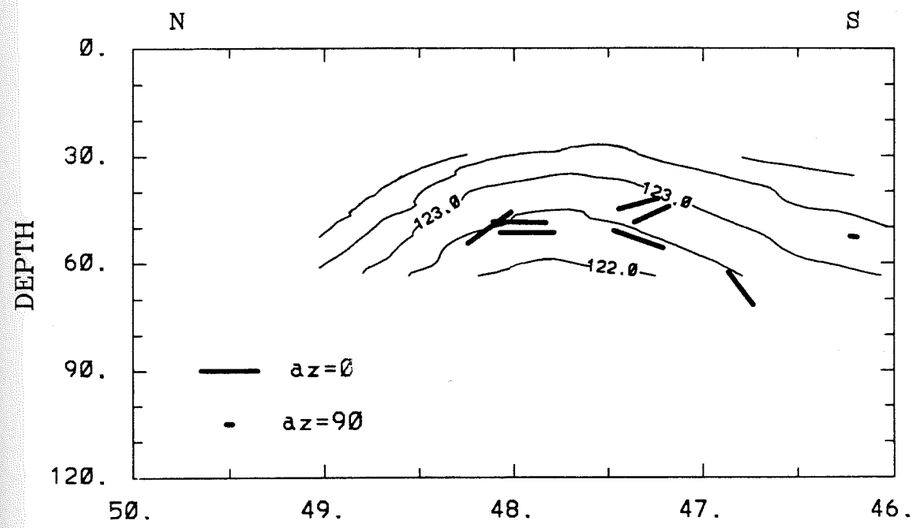

Figure 5.2. T axes of the higher magnitude events in the slab plotted in a north-south cross-section. The contours are equal longitude curves representing the arched slab.

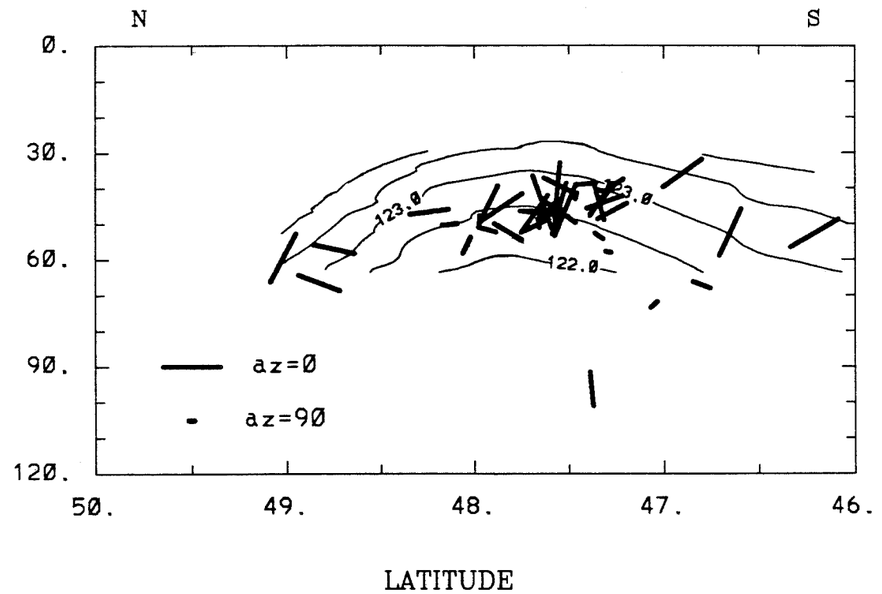

Figure 5.3. P axes of the slab earthquakes plotted in a north-south cross-section. Contours are equal longitude curves representing the arched slab.

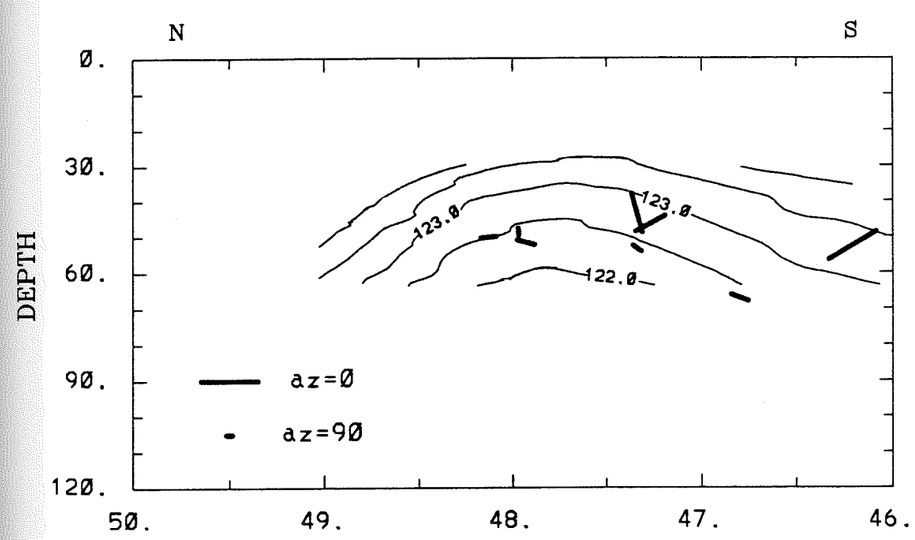

Figure 5.4. P axes of the higher magnitude events in the slab plotted in a north-south cross-section. The contours are equal longitude curves representing the arched slab.

BIBLIOGRAPHY

Algermissen, S. T. and S. T. Harding, The Puget Sound, Washington earthquake of April 29, 1965 - Preliminary seismology report, 1965.

Angelier J., J. F. Dumont, H. Kalamanderesi, P. Poisson, and S. Simsek, Analyses of fault mechanisms and expansion of southwestern Anatolia since the late Miocene, *Tectonophysics* **75**, T1-T9, 1981a.

Angelier, J., B. Colletta, J. Chorowicz ,L. Ortlieb, and C. Rangin, Fault tectonics of the Baja California Peninsula and the opening of the Sea of Cortez, Mexico, *J. Struct. Geol.,* **3**, 347-357, 1981b.

Angelier, J. A., B. Valette, and S. Manousis, Inversion of field data in fault tectonics to obtain the regional stress, 1. Single phase fault populations: A new method of computing the stress tensor, *Geophys. J. R. Astron. Soc.,* **69**, 607-621, 1982.

Armijo R., E. Carey, and A. Cisternas, The inverse problem in microtectonics and the separation of tectonic phases, *Tectonophysics* **82**, 145-161, 1982.

Atwater, T., Implications of plate tectonics for the Cenozoic tectonic evolution of western North America, *Geol. Soc. Am. Bull.,* **81**, 3513-3536, 1970.

Claerbout, J. F. and F. Muir, Robust modeling with erratic data, *Geophsics,* **38**, 826-844, 1973.

Crosson, R. S., Small earthquakes, structure, and tectonics of the Puget Sound region, *Bull. Seis. Soc. Am.,* **62(5)**, 1133-1177.

Crosson, R. S. and D. Frank, The Mt. Rainier earthquakes of July 18, 1973 and its tectonic significance, *Bull. Seis. Soc. Am.,* **65**, 393-401, 1975.

Crosson, R. S. and J. W. Lin, A note on the Mt. Rainier earthquake of April 20, 1974, *Bull. Seis. Soc. Am.,* **65**, 549-556, 1975.

Crosson, R. S., Crustal structure modeling of earthquake data 2. Velocity structure of the Puget Sound region, Washington, *J. Geophys. Res.* **81**(17), 3047-3054, 1976.

Crosson, R. S., Review of seismicity in the Puget Sound region from 1970 through 1978, in *Proceedings of Workshop XIV, Earthquake Hazards of the Puget Sound Region, Washington,* edited by J. C. Yount, 1983. USGS open file report, 6-18.

Crosson, R. S. and T. J. Owens, Slab geometry of the Cascadia subduction zone beneath Washington from earthquake hypocenters and teleseismic converted waves, *Geophys. Res. Lett.,* In press, 1987.

Ellsworth, W. L. and X. Zhonghuai, Determination of the stress tensor from focal mechanism data, *EOS Trans. AGU.,* **61**, 1117, 1980.

Etchecopar, A., G. Vasseur, and M. Daignieres, An inverse problem in microtectonics for the determination of stress tensors from fault striation analysis, *J. Struct. Geol.,* **3**, 51-65, 1981.

Gephart, J. W. and D. W. Forsyth, An improved method for determining the regional stress tensor using earthquake focal mechanism data: Application to the San Fernando earthquake sequence, *J. Geophys. Res.,* **89**, 9305-9320, 1984.

Grant, W. C., C. S. Weaver, and J. E. Zollweg, The 14 February 1981 Elk Lake, Washington earthquake sequence, *Bull. Seis. Soc. Am.,* **74**, 1289-1309, 1984.

Green, A. G., R. M. Clowes, C. J. Yorath, C. Spencer, E. R. Kanasewich, M. T. Brandon, and A. S. Brown, Seismic reflection imaging of the subducting Juan de

Fuca plate, *Nature,* **319**, 210-213, 1986.

Heaton, T. H. and H. Kanamori, Seismic potential associated with subduction in the Northwestern United States, *Bull. Seis. Soc. Am.,* **74**(3), 933-941, 1984

Hodgson, J. H. and R. S. Storey, Direction of faulting in some of the large earthquakes of 1949, *Bull. Seis. Soc. Am.,* **44**, 57-83, 1954.

Isacks, B. and P. Molnar, Distribution of stresses in the descending lithosphere from a global survey of focal mechanism solutions of mantle earthquakes, *Revs. Geophy. and Space Phys.,* **9**, 103-174, 1971.

Keach, R. W., C. J. Potter, J. E. Oliver, and L. D. Brown, Cenozoic active margin and shallow Cascades structure: COCORP results from western Oregon (abstract), *GSA Annual Meet.,* **652**, 1986.

Langston, C. A. and D. E. Blum, The April 29, 1965, Puget Sound earthquake and the crustal and upper mantle structure of western Washington *Bull. Seis. Soc. Am.,* **67**, 693-711, 1977.

LePichon, X., J. Francheteau, and J. Bonnin, *Plate Tectonics, pp. 300, Elsevier, New York, 1973.*

Lisowski, M. and J.C. Savage, Geodetic strain in northwestern Washington, manuscript in preparation, 1987.

Malone, S. D., G.H. Rothe, and S.W. Smith, Details of microearthquake swarms in the Columbia Basin, Washington, *Bull. Seis. Soc. Am.* **65**, 4, 855-864, 1975.

Mardia, K. V., *Statistics of direction data, pp. 212-222, Acdemic Press, New York, 1972.*

Mckenzie, D. P., The relation between fault plane solutions for earthquakes and the directions of the principal stresses, *Bull. Seis. Soc. Am.*, **59**(2), 591-601, 1969.

Parker, R. L., and M. K. McNutt, Statistics for the one-norm misfit measure, *J. Geophys. Res.*, **85**, 4429-4430, 1980.

Qamar, A., A. Rathbun, R. Ludwin, L.L. Noson, R. S. Crosson, and S. D. Malone, *Earthquake hypocenters in Washington and Northern Oregon - 1981, Washington Dept. of Natural Resources, Division of Geology and Earth Resources, 1987.*

Qamar, A. R. Ludwin, R. S. Crosson, and S. D. Malone, *Earthquake hypocenters in Washington and Northern Oregon - 1982-1986, Washington Dept. of Natural Resources, Division of Geology and Earth Resources, 1987.*

Riddihough, R. P., Recent movements of the Juan de Fuca plate system, *J. Geophys. Res.*, **89**(B8), 6980-6994, 1984.

Rogers, G. C., Earthquake fault plane solutions near Vancouver Island, *Can. J. Earth Sci.*, **16**, 523-531, 1979.

Savage, J. C., M. Lisowski, and W. H. Prescott, Geodetic strain measurements in Washington, J. Geophys. Res., **86**(B6), 4929-4940, 1981.

Sbar, M. L., Delineation and interpretation of seismotectonic domains in western North America, *J. Geophys. Res.*, **87**, 3919-3928, 1982.

Sbar, M. L., An explanation for contradictory geodetic strain and fault plane solution data in western North America, *Geophys. Res. Letters,* **10**(3), 177-180, 1983.

Taber, J. John and S. W. Smith, Seismicity and focal mechanisms of the Juan de Fuca plate beneath the Olympic Peninsula, Washington, *Bull. Seis. Soc. Amer.*, **75**, 237-249, 1985.

Weaver, C. S. and S. W. Smith, Regional tectonic and earthquake hazard implications of a crustal fault zone in southwestern Washington, *J. Geophys. Res.*, **88**(B12), 10,371-10383, 1983.

Yelin, T. S., *The Seattle earthquake swarms and Puget Basin focal mechanisms and their tectonic implications,*
Univ. of Washington, 1982. M.S. Thesis.

Yelin, T. S. and R. S. Crosson, A note on the south Puget Sound basin magnitude 4.6 earthquake of 11 March 1978 and its aftershocks, *Bull. Seis. Soc. Am.*, **72**, 1033-1038, 1982.

Zoback, M. L. and M. Zoback, State of stress in the conterminuos United States, *J. Geophys. Res.* **85**, 6113-6156, 1980.

Appendix

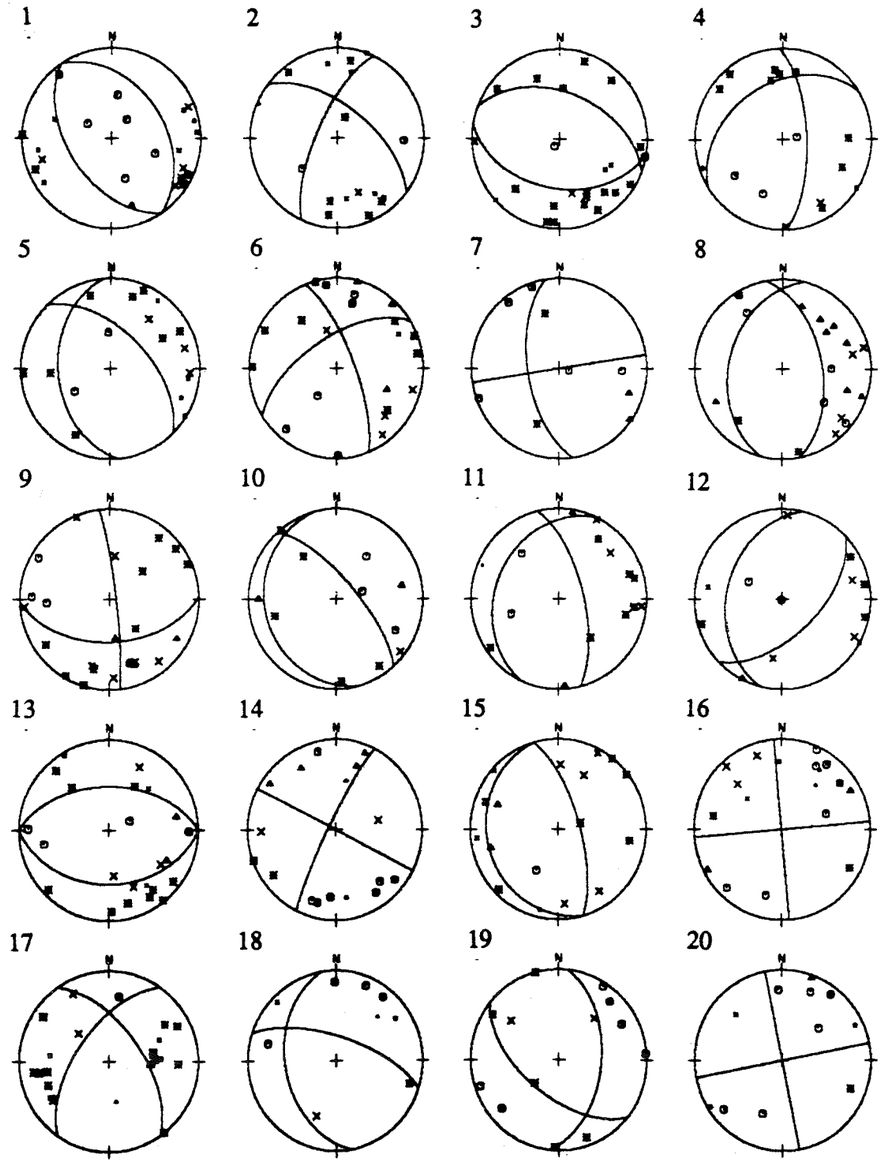

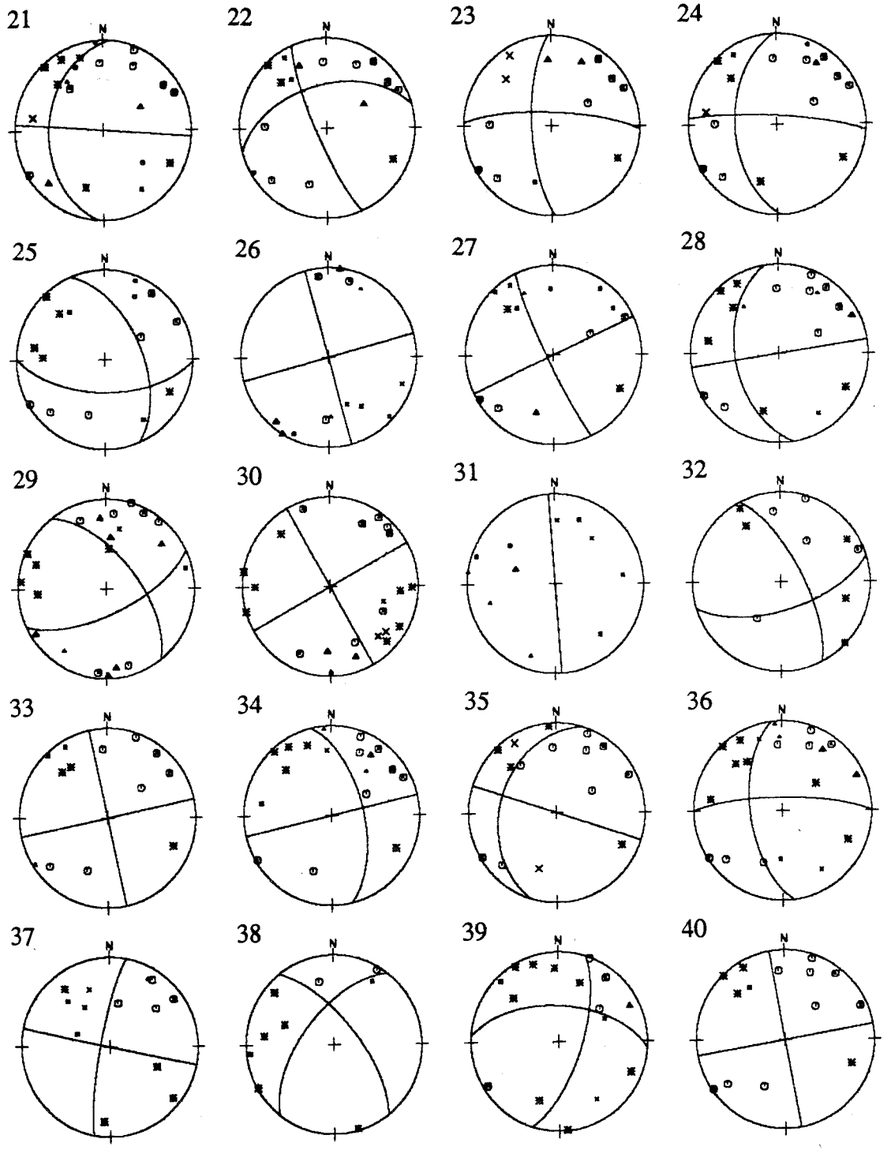
21
22
23
24
25
26
27
28
29
30
31
32
33
34
35
36
37
38
39
40
N

41
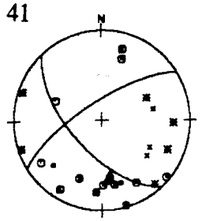
42
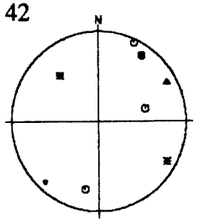
43
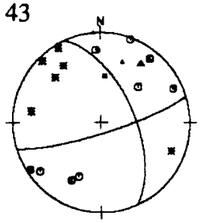
44
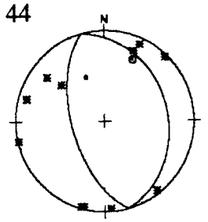
45
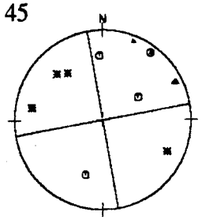
46
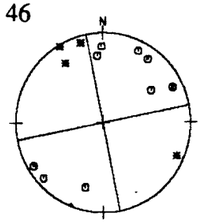
47
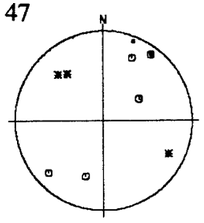
48
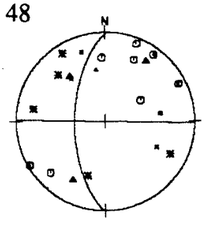
49
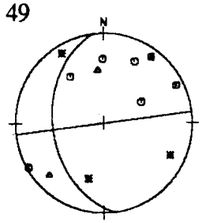
50
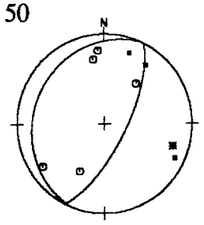
51
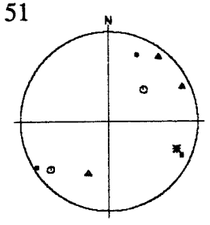
52
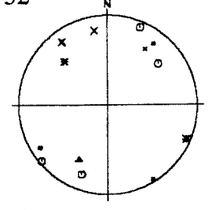
53
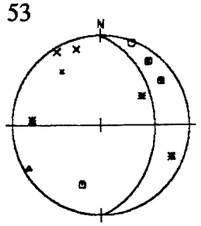
54
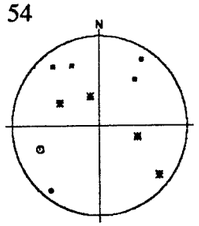
55
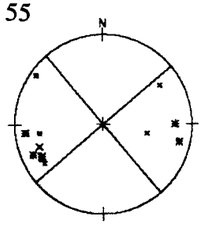
56
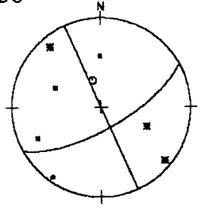
57
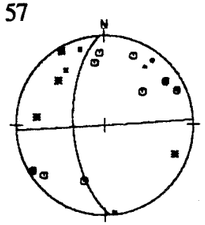
58
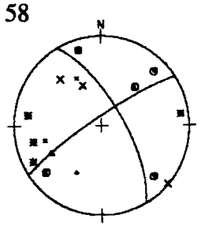
59
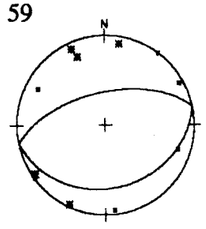
60
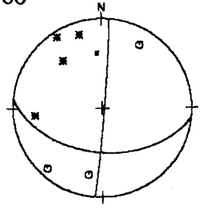

61

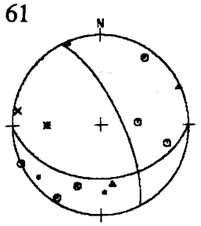

62

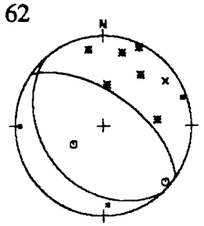

63

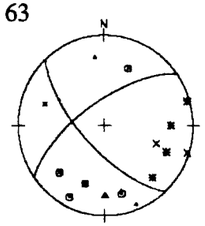

64

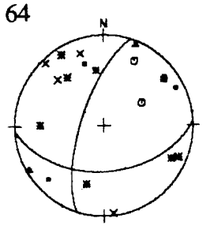

65

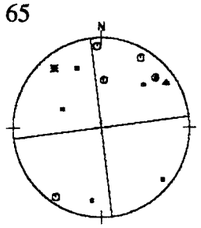

66

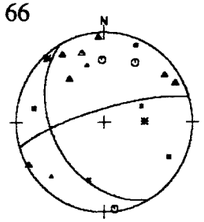

67

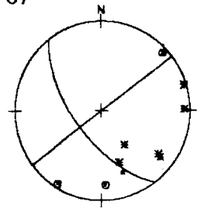

68

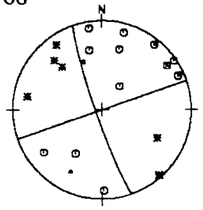

69

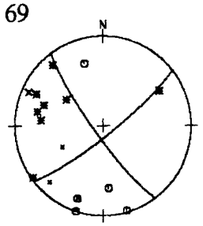

70

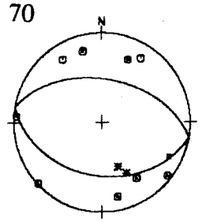

71

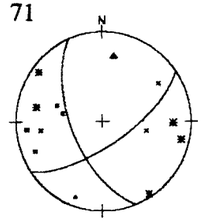

72

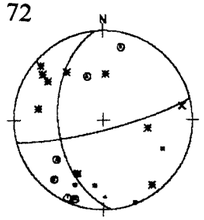

73

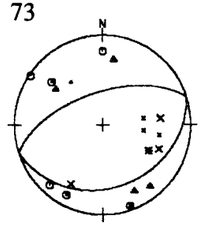

74

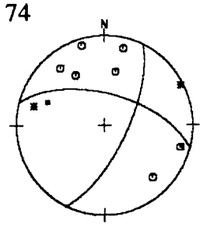

75

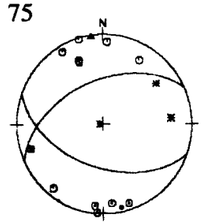

76

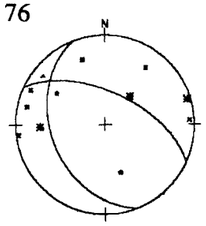

77

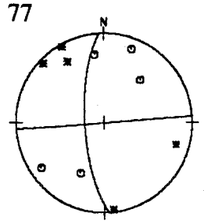

78

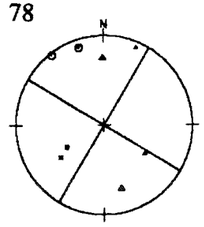

79

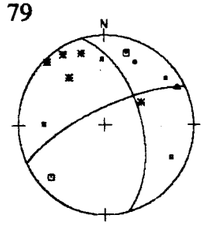

80

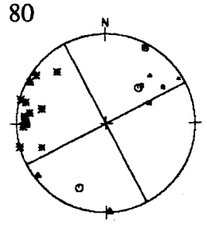

81
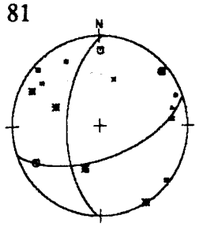
82
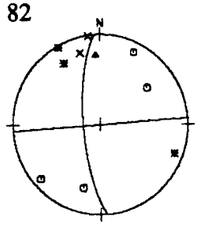
83
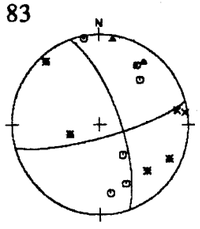
84
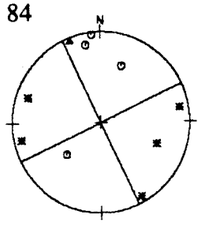
85
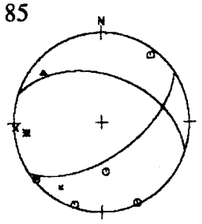
86
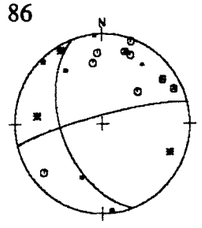
87
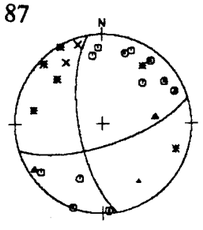
88
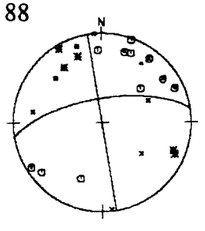
89
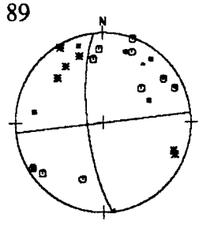
90
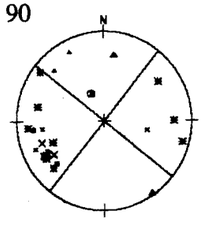
91
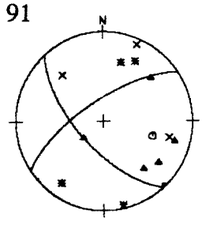
92
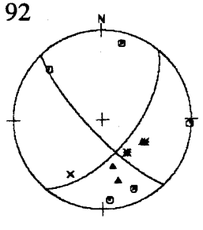
93
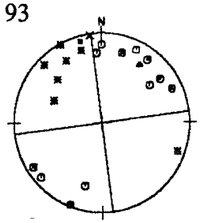
94
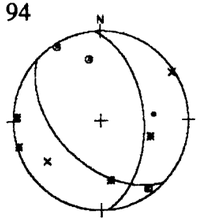
95
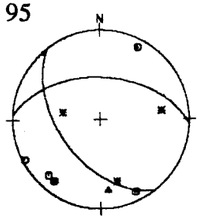
96
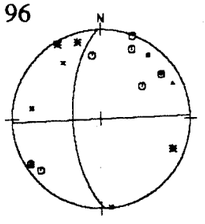
97
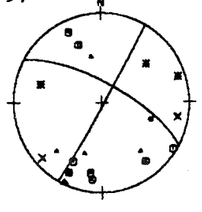
98
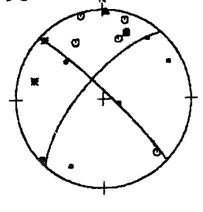
99
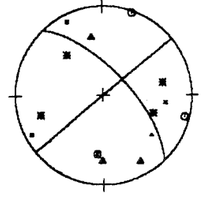
100
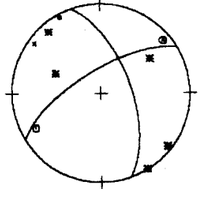

101
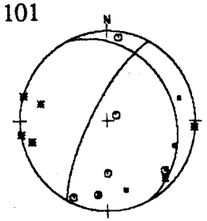
102
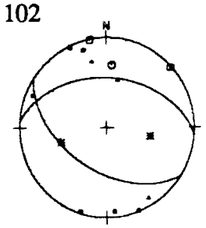
103
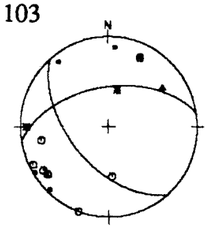
104
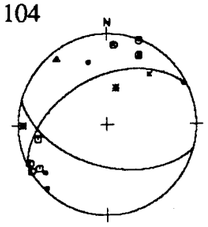
105
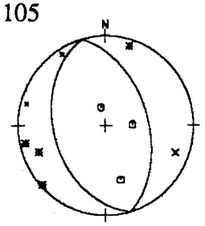
106
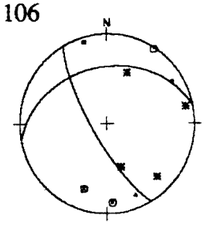
107
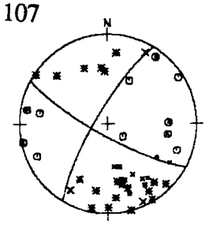
108
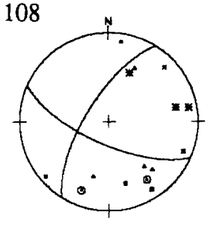
109
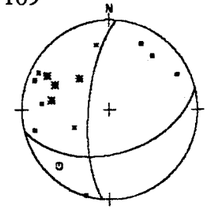
110
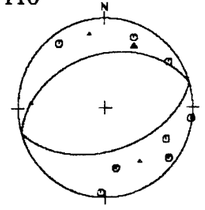
111
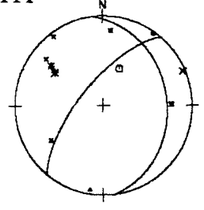
112
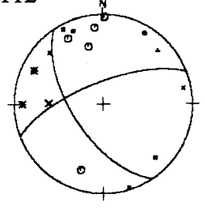
113
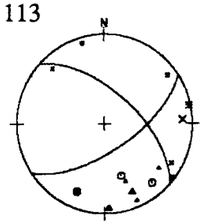
114
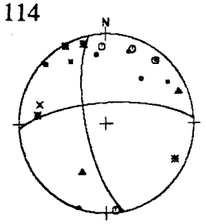
115
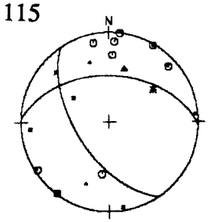
116
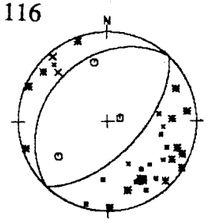
117
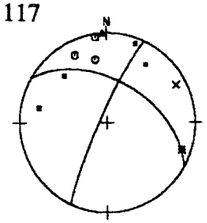
118
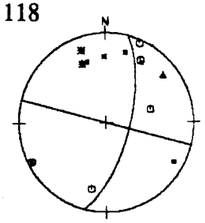
119
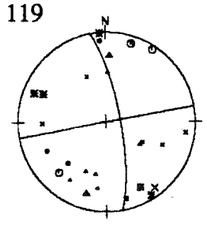
120
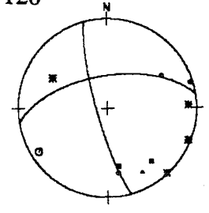

121

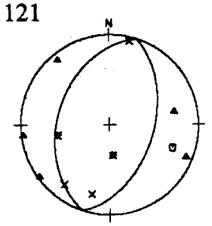

122

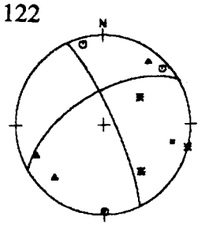

123

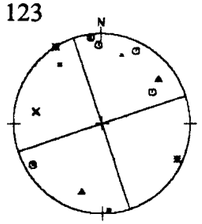

124

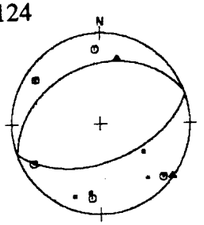

125

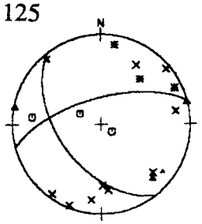

126

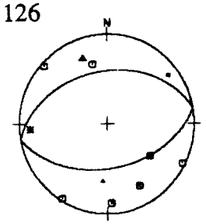

127

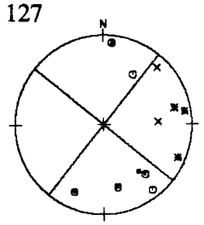

128

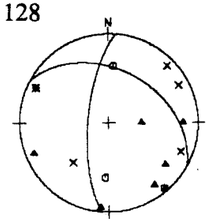

129

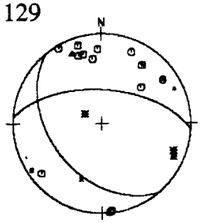

130

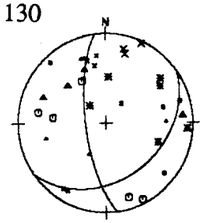

131

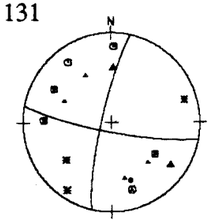

132

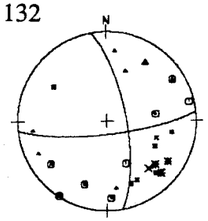

133

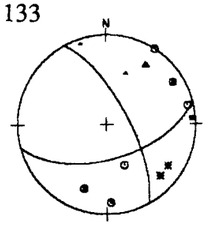

134

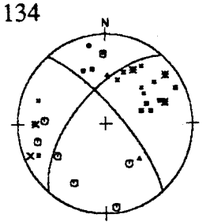

135

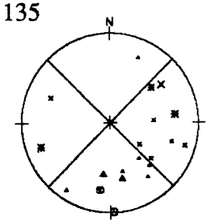

136

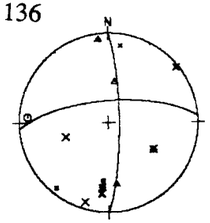

137

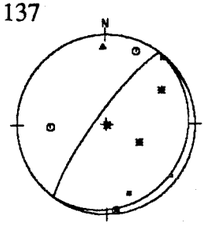

138

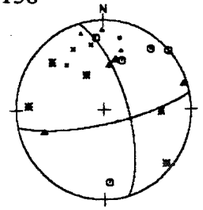

139

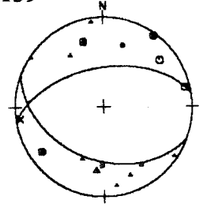

140

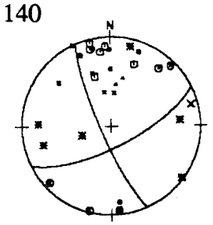

141 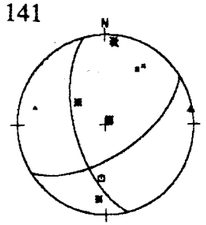

142 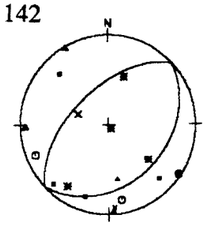

143 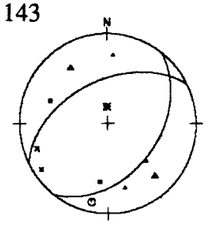

144 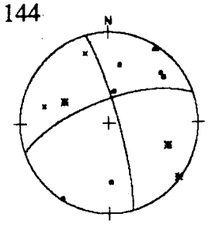

145 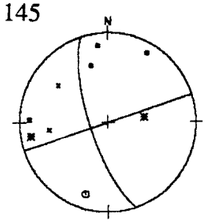

146 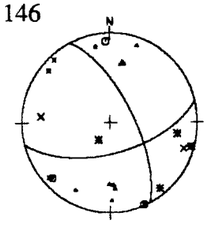

147 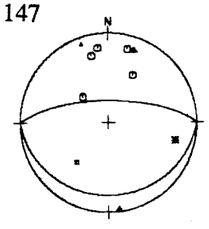

148 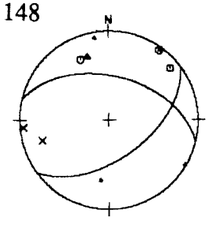

149 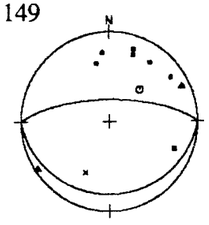

150 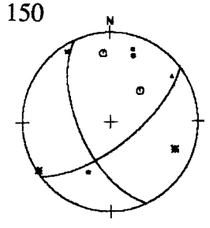

151 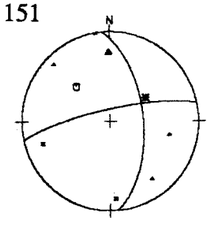

152 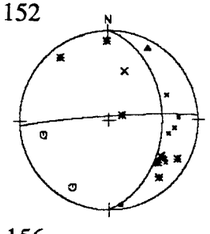

153 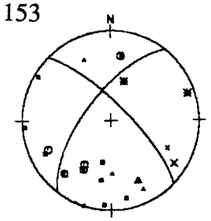

154 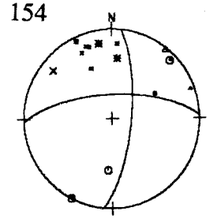

155 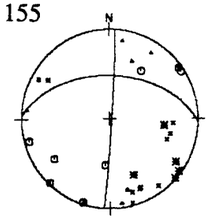

156 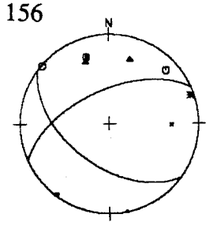

157 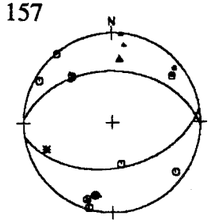

158 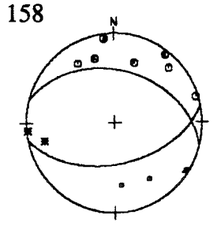

159 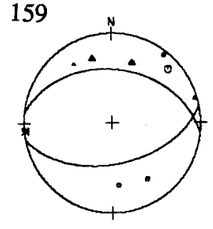

160 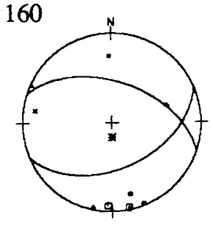

161
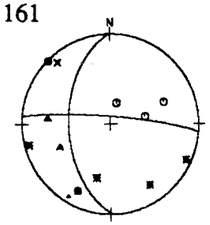
162
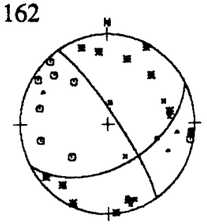
163
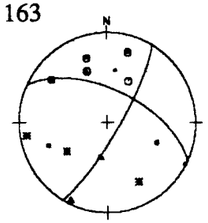
164
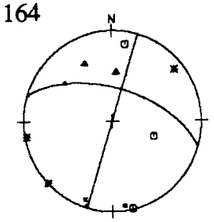
165
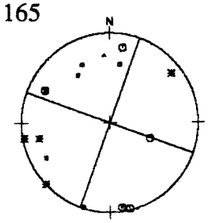
166
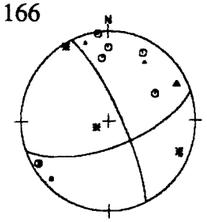
167
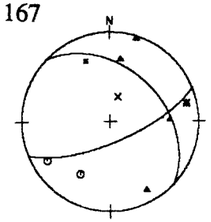
168
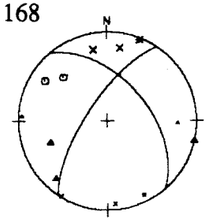
169
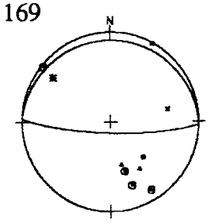
170
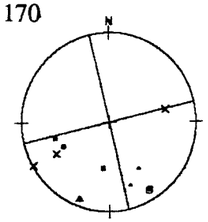
171
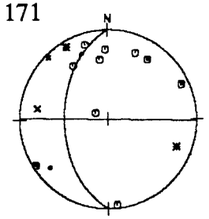
172
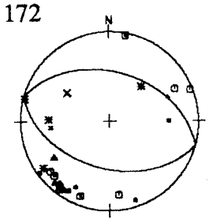
173
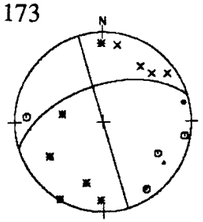
174
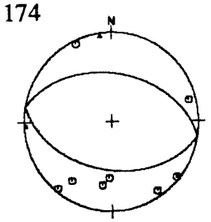
175
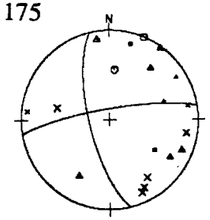
176
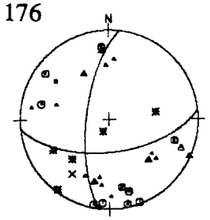
177
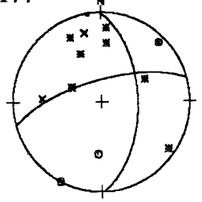
178
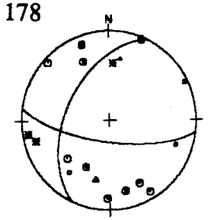
179
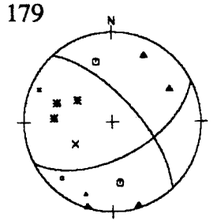
180
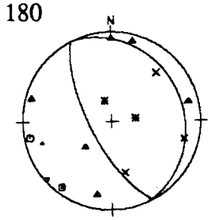

181

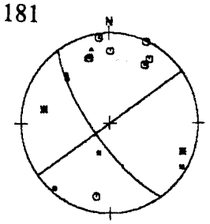

182

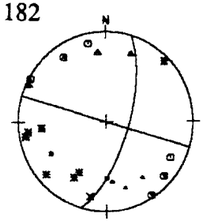

183

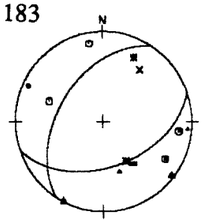

184

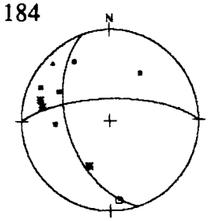

185

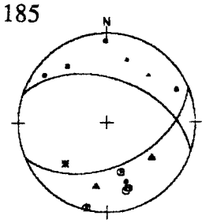

186

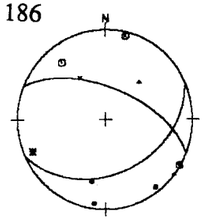

187

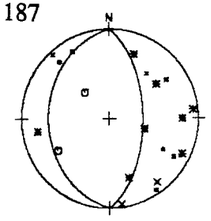

188

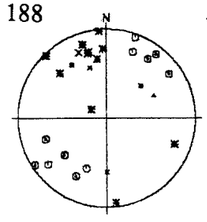

189

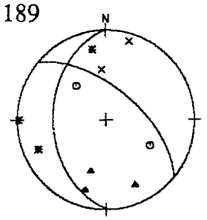

190

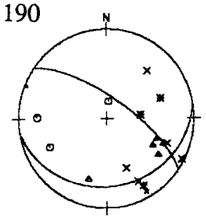

191